RETRIEVAL OF WATER-ICE CLOUD OPACITY AT THE PHOENIX MARS LANDING SITE FROM RADIATIVE TRANSFER IN THERMAL AND VISIBLE WAVELENGTHS

GRACE BISCHOF

A THESIS SUBMITTED TO THE FACULTY OF GRADUATE STUDIES
IN PARTIAL FULFILMENT OF THE REQUIREMENTS
FOR THE DEGREE OF

MASTER OF SCIENCE

GRADUATE PROGRAM IN PHYSICS AND ASTRONOMY
YORK UNIVERSITY
TORONTO, ONTARIO

AUGUST 2022

© GRACE BISCHOF, 2022

Abstract

Water-ice clouds at the Phoenix landing site are investigated by considering radiative transfer in thermal and visible wavelengths. First, we reconstruct a record of water-ice clouds at the Phoenix landing site by examining the radiative contribution to the surface energy balance and compare our results to the Phoenix lidar. We find that clouds, radiating between 0 and 30 W m^{-2}, were present earlier in the mission than previously known and that optically thicker clouds emitted more radiation toward the surface. Next, we use a doubling-and-adding radiative transfer model to derive the visible opacities of the water-ice clouds in images. The derived opacities are consistent with prior studies during the daytime, but give higher opacities between 2:00 - 10:00 LTST. This work allows us to make a direct comparison between the visible opacity of the cloud and the thermal radiation emitted by the cloud to better constrain their effect on the atmosphere.

Table of Contents

List of Tables

List of Figures

Chapter 1

Introduction

1.1 Introduction to the Martian Atmosphere

From a thick, warm and moist atmosphere billions of years ago to a thin, dry, and cold climate, the Martian atmosphere remains a dynamic and variable component of the planet. Earth-based telescopes, instruments orbiting around Mars, and landers on the surface all work in an effort to understand the processes driving the climate, chemistry, and dynamics of the atmosphere of Mars. Understanding atmospheric processes on Mars gives insight into the history of the planet, the viability of past and present life on the surface, and the potential for future human exploration.

The thin atmosphere of current-day Mars is primarily composed of CO_2, with trace amounts of other gases, including water vapour (Summers et al., 2002). With an obliquity of 25.2°, Mars experiences seasons similarly to Earth, with changes in weather and daylight hours between the northern and southern hemispheres (Martínez et al., 2017). Exceptionally, Mars' high eccentricity contributes to two distinct atmospheric phenomena. At perihelion, an increase in global temperature contributes to dust lifting, with the potential for planet-encircling dust storms (Cantor et al., 2001; Guzewich et al., 2019). During aphelion, cooler temperatures lead to increased water-ice cloud formation (Clancy et al., 1996; Christensen et al., 2001).

Seasons on Mars are tracked using a convention called "solar longitude" (L_s), which indicates the position of the planet in its orbit around the sun. Conventionally, $L_s = 0°$ corresponds with northern vernal equinox, $L_s = 90°$ is northern summer solstice, followed by northern autumnal equinox and northern winter solstice at $L_s = 180°$ and $L_s = 270°$, respectively. One full orbit of the planet around the sun takes 686 Earth days, or 668 sols, where a sol is 24 hours and 39 minutes long.

The atmosphere of Mars is split into multiple layers, including the troposphere, mesosphere, and thermosphere. The lowest few kilometres of the troposphere is called the Planetary Boundary Layer (PBL), shown in Figure 1.1. The PBL is the layer of atmosphere which interacts with, and is influenced by, the surface. Strong convection and vertical mixing occur in the PBL during the day, with a height up to 10 km (Petrosyan et al., 2011). At night, the PBL collapses into a shallow layer with low diffusivity and low turbulence (Guzewich et al., 2017).

The PBL is an important aspect of the Martian atmosphere because it is where the bulk of heat and mass transport occurs. As such, understanding atmospheric processes relies on a thorough understanding of the PBL. By studying the activities occurring in the PBL —namely, cloud, dust, and gas processes —we can begin to understand the climate and evolution of the atmosphere of Mars. This thesis will focus specifically on better understanding clouds by examining data from the Phoenix Mars mission.

1.2 Martian Water-Ice Clouds

Despite the small amount of water vapor in the Martian atmosphere, water-ice clouds are a reoccurring atmospheric phenomena on Mars. Clouds on Mars have been viewed from

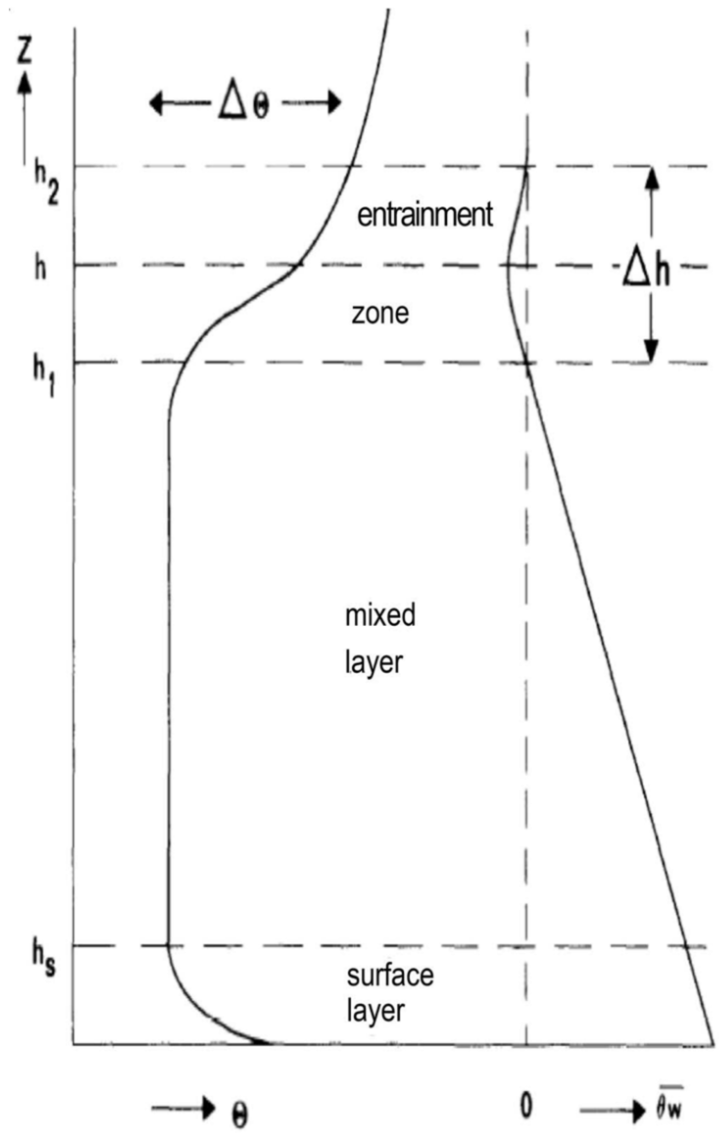

Figure 1.1: From (Petrosyan et al., 2011), depicting the layers of the PBL. The PBL is where the surface and near-surface atmosphere interact, resulting in mass and heat transport between the two. Understanding surface-atmosphere interactions is crucial for properly characterizing atmospheric dynamics.

early ground-based telescopic observations (Dollfus, 1957; Pollack and Sagan, 1969), with a visible-wavelength image shown in Figure 1.2, and have since been studied by a variety of instruments, from Martian orbiters (Vago et al., 2015; Schmidt, 2003; Graf et al., 2005), to landers and rovers on the surface of Mars (Taylor et al., 2008; Grotzinger et al., 2012; Farley et al., 2020). Here, we will walk through some of the observations of water-ice clouds on Mars.

Water-ice clouds form on Mars when water vapour nucleates onto condensation nuclei – typically dust, or other particulates in the Martian atmosphere (Määttänen and Montmessin, 2021). Water-ice clouds form in several latitudes of Mars throughout a Martian Year (MY), as local temperatures become cool enough in a saturated environment for water vapour to condense to form ice-crystals (Richardson et al., 2002). Studying the clouds in several locations on Mars gives insight into the behaviour and microphysical properties of clouds, including the seasonal and diurnal cycles, and optical depths of the clouds.

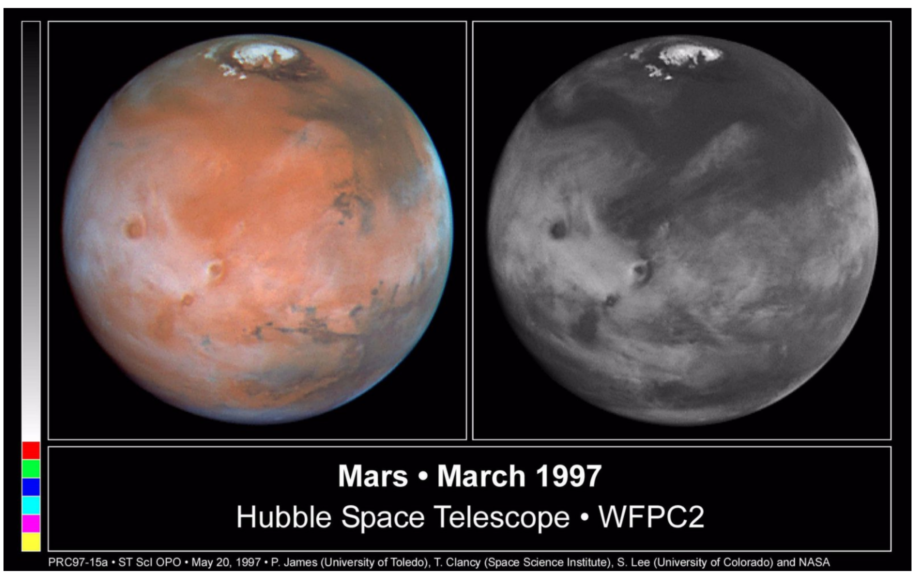

Figure 1.2: Taken with the Hubble Space Telescope in 1997, the left and right image show Martian clouds while the planet is in its aphelion position. The left image is taken in red (673 nm), green (502 nm) and blue (410 nm) wavelengths. The right image is only in blue, bringing out the contrast between the clouds and the surface of the planet. The global coverage of clouds impacts the climate of the planet. Image Credit: JPL/NASA/STScI

In the equatorial region of Mars, a belt of water-ice clouds forms when the planet is furthest from the sun. Aptly named the “Aphelion Cloud Belt” (ACB), this time of year sees an enhancement in water-ice cloud formation with a strong yearly repeatability (Clancy et al., 1996). The ACB has been studied by many instruments, including from Mars' orbit using the Thermal Emission Imaging System (THEMIS) on the Mars Odyssey orbiter, where water-ice optical depths are shown to increase to 0.15 at $L_s = 90°$ (Smith, 2019).

An important mission in characterizing ACB clouds is the Mars Science Laboratory (MSL; Curiosity Rover), which landed in Gale Crater in 2012 (Grotzinger et al., 2012). The Curiosity rover uses several cameras to image the sky, with the Navigation Camera (NavCam) being used specifically for cloud studies. A study into the diurnal variability of the clouds in Gale Crater showed enhanced opacity in the morning and lower opacity in the afternoons (Kloos et al., 2018). The microphysical properties of the ACB clouds were investigated by examining the scattering phase function of the clouds (Cooper et al., 2019). Cooper et al. (2019) found the likely ice-crystal geometry composing the clouds are aggregates, hexagonal solid columns, hollow columns, plates, and bullet rosettes, with spheres and cylinders being possible but unlikely.

In early northern autumn, the Mars Climate Sounder (MCS) instrument on the Mars Reconnaissance Orbiter (MRO), observes an increase in water-ice clouds northward of 60°N. Known as the Polar Hood Clouds (Martin and McKinney, 1974), these water-ice clouds are shown to form around $L_s = 150°$ and dissipate by $L_s = 30°$, with higher optical depths in the nighttime than the daytime (Benson et al., 2011). A similar multi-year analysis using the Mars Global Surveyor (MGS) Thermal Emission Spectrometer (TES) saw the polar hood clouds linger until $L_s = 75°$ (Tamppari et al., 2008), which may be explained by the TES seeing further down into the atmosphere than MCS, capturing clouds lower to the surface. In the late spring to early summer, TES captured sporadic water-ice clouds with low optical depths during the daytime (Tamppari et al., 2008).

Another repeatable cloud phenomena occurring in the northern polar region is the formation of the annular cloud. The annular cloud has been imaged extensively from orbit, using both MRO and the Mars Express (MEx) orbiters (Sánchez-Lavega et al., 2018). An image of the annular cloud can be seen in Figure 1.3. The annular cloud forms at a latitude around 60°N at a solar longitude of $L_s = 120°$, with high year-to-year repeatability in occurrence, but with inter-annual variability in appearance and dynamics, potentially due to variability in dust loading in the atmosphere (Sánchez-Lavega et al., 2018).

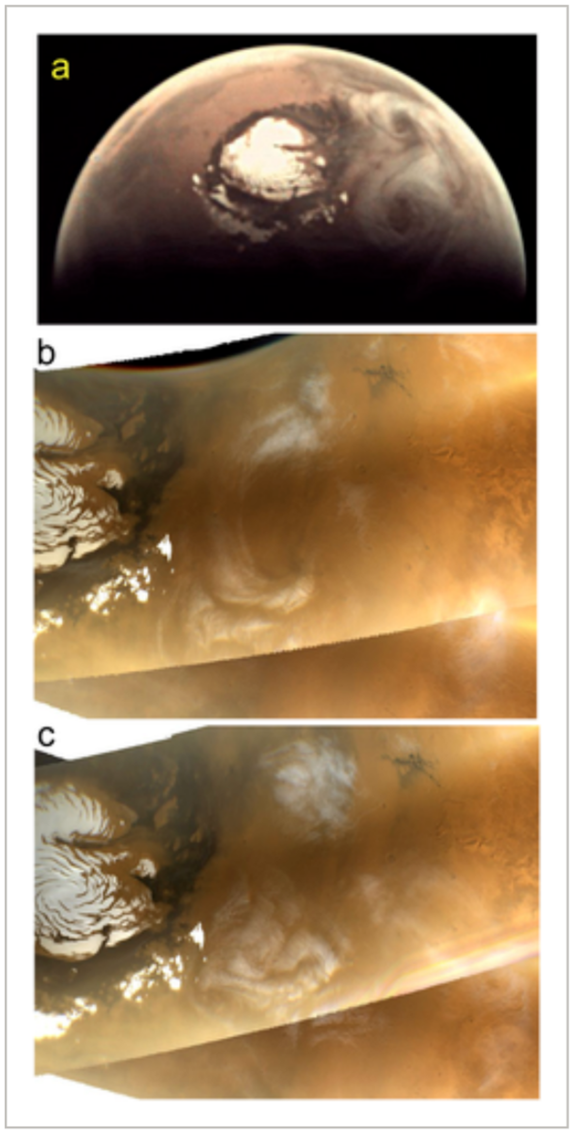

Figure 1.3: The annular cloud as seen from MEx on (a) June 18, 2012 (b) June 19, 2012 and (c) June 20, 2012. A double cyclone was observed in this year. Image credit: Sánchez-Lavega et al. (2018)

The formation of the annular cloud occurs when the water vapour abundance in the Martian atmosphere reaches its annual peak (Tamppari et al., 2010; Tyler and Barnes, 2014). In the early hours of the day, as the temperature lowers, the annular cloud forms, whereas warming in the morning breaks up the cloud (Sánchez-Lavega et al., 2018). In addition to the inter-annual variability, the annular cloud displays a high degree of sol-to-sol variability.

1.3 Interaction between Clouds and Radiation

The presence of water-ice clouds has key implications for the Martian weather and climate. While the effects of water-ice clouds were initially not well known, over the years insight has been gained into their role in the water cycle, transporting water vapour between hemispheres (Montmessin et al., 2004; Tamppari et al., 2003), as well as their role as meteorological markers for frost-point temperature, humidity, and winds (Wilson et al., 2007; Madeleine et al., 2012; Moores et al., 2010).

An important way clouds affect the climate is by their interaction with radiation. During a Martian sol, the diurnal temperature can fluctuate by over 70 K between the maximum and minimum temperatures (Martínez et al., 2017). Despite the Martian atmosphere containing mostly CO_2 – an abundant greenhouse gas on Earth – Mars does not experience a large greenhouse effect due to the atmosphere being extremely thin. As such, the diurnal temperature is largely driven by incoming solar radiation from the sun and outgoing thermal radiation from the surface (Savijärvi, 2014).

Atmospheric aerosols have been shown to affect the weather on Mars due to their radiative impact. Dust, for example, is a main driver of the climate of Mars (Madeleine et al., 2011). Dust affects the atmosphere by scattering incoming solar radiation and absorbing longwave radiation from the surface. During the MY 34 Global Dust Storm, the enhanced dust measured by the MSL rover resulted in suppressed diurnal temperature ranges by up to 30 K due to a 97% decrease in incident ultraviolet light (Guzewich et al., 2019). Dust, however, is not the only atmospheric aerosol with such properties. Ice crystals formed in water-ice clouds can produce similar atmospheric temperature effect. A simplified version of this surface energy balance is shown in Figure 1.4.

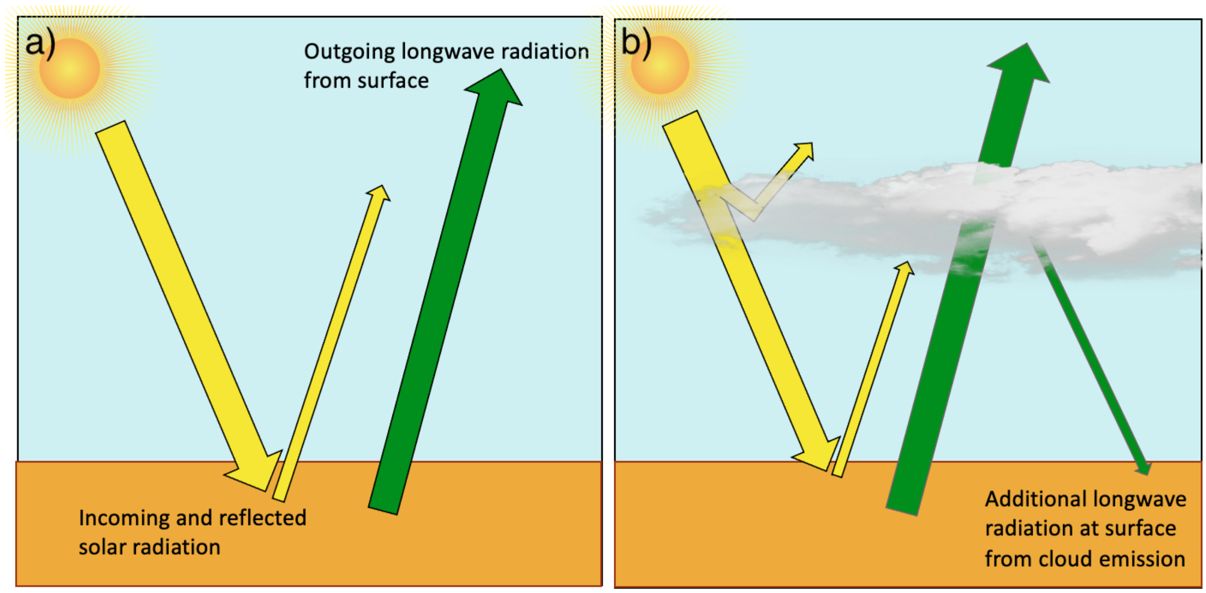

Figure 1.4: Simplified schematic of the surface energy balance (a) without and (b) with clouds. When no clouds are present, the temperature is driven by the balance of incoming shortwave radiation and outgoing longwave radiation. When clouds are present, the clouds absorb a portion of the outgoing longwave radiation, thermally re-emitting the radiation back toward the surface.

As with dust, the two main ways water-ice clouds interact with radiation is through the scattering of shortwave radiation and absorption and re-emission of longwave radiation. As water vapour condenses to form ice crystals in the atmosphere, latent heat is emitted from the cloud due to the change in phase (Kuo, 1961). Because of these two processes, the presence of water-ice clouds can both cool and warm the atmosphere. During the daytime, if a cloud is optically thick, the cloud scatters more incident radiation than it makes up by thermal re-emittance. The decrease in the flux received at the surface results in cooler surface and near-surface atmospheric temperatures. Alternatively, when clouds thermally emit more radiation than they scatter, the net increase in flux at the surface causes temperatures to increase. This has been well documented on Earth with low, thick clouds decreasing temperatures and high, thin clouds increasing temperatures, particularly in the nighttime (Hong et al., 2016).

This phenomena has been modelled on Mars, using General Circulation Models (GCMs) to model the effect of radiatively-active water-ice clouds (Colaprete and Toon, 2000; Hinson and Wilson, 2004; Wilson et al., 2007; Wilson and Guzewich, 2014). In particular, when modelling nighttime air temperatures in the Tharsis Region, the temperatures were better matched when radiatively-active water-ice clouds were added to the GCM (Wilson et al., 2007). Wilson et al. (2007) concluded that clouds with an opacity > 1 provided enough downwelling IR flux to account for observed temperature anomalies.

Recently, anomalies were noted in the ground and air temperatures recorded by the Curiosity Rover (Grotzinger et al., 2012), where a local peak in the daily minimum temperature occurs as the planet approaches its aphelion position (Cooper et al., 2021). Cooper et al. (2021) explored the formation of water-ice clouds in the evening and throughout the night as a mechanism for increasing the daily minimum air temperature. Nighttime clouds present throughout the ACB season prevent the escape of thermal radiation, re-radiating the energy back toward the surface. Nighttime atmospheric thermal emission was shown to increase by 10 W m^{-2} in the cloudy season compared to the dusty season, as seen in Figure 1.5, illustrating that clouds produce a marked effect on the temperature and surface energy balance (Cooper et al., 2021).

Due to the impact water-ice clouds have on the climate, constraining a cloud's micro-physical properties is crucial for assessing their full radiative impact. One such property, as highlighted in Wilson et al. (2007), is the cloud opacity, which will affect the amount of downwelling longwave flux given off by the cloud. Thus, we must define "optical depth" and how it relates to the atmosphere.

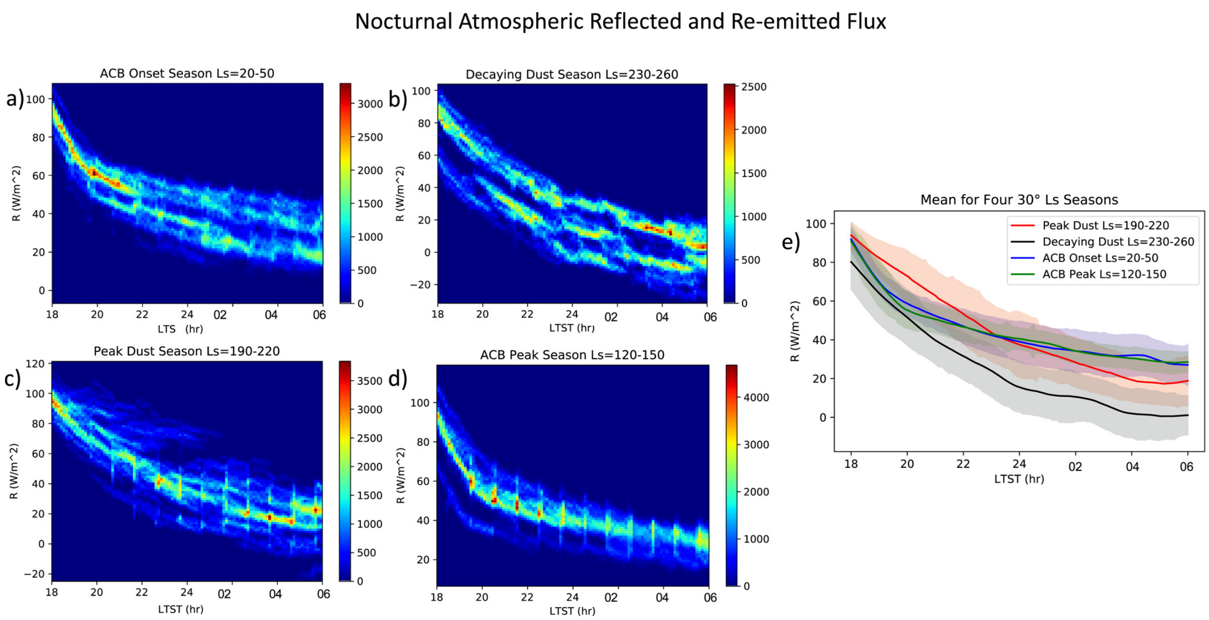

Figure 1.5: Image from (Cooper et al., 2021), showing that during the dusty season, the amount of reflected and re-emitted flux coming from the atmosphere is lower than during the ACB season. The reflected and re-emitted flux is higher at this time, explaining the perturbation seen in the temperature data.

First, we begin by discussing the attenuation of light in an atmosphere. Along an infinitesimal path, ds, the attenuation of light, dI_λ, will vary according to the extinction and emission occurring along the path. This is represented as

$$dI_\lambda = -k_\lambda(s)\rho(s)I_\lambda ds + k_\lambda \rho(s) J_\lambda ds \tag{1.1}$$

where k_λ is the extinction coefficient which represents both scattering and absorption, $\rho(s)$ is the density of the material along the path, I_λ is the spectral radiance, J_λ is the source term representing the emission of radiation, and ds is the optical path. This equation can be simplified to

$$\frac{dI_\lambda}{ds} = -k_\lambda(s)\rho(s)(I_\lambda - J_\lambda) \tag{1.2}$$

which is also known as the radiative transfer equation or the Schwarzschild equation.

From here, we can define the optical depth as

$$\begin{aligned}
\tau &= \int_{s_0}^{s} k_\lambda(s)\rho(s)ds \\
d\tau &= k_\lambda \rho(s)ds
\end{aligned} \tag{1.3}$$

and the Schwarzschild equation can be written as

$$\frac{dI_\lambda}{d\tau} = -I_\lambda + J_\lambda \tag{1.4}$$

If we assume no source term, the Schwarzschild equation can be simplified to

$$\begin{aligned}
\frac{dI_\lambda}{d\tau} &= -I_\lambda \\
\int_{I_0}^{I} \frac{dI_\lambda}{I_\lambda} &= \int_0^\tau d\tau \\
ln\frac{I}{I_0} &= -\tau \\
I &= I_0 e^{-\tau}
\end{aligned} \tag{1.5}$$

If a material has an optical depth much greater than 1, the material is said to be optically thick, and light will not easily pass through the material, instead being absorbed and scattered. An optically thin material, with an optical depth less than 1, will allow light to easily pass through.

Since aerosols in the Martian atmosphere scatter, absorb, and emit radiation, understanding the balance between the scattering of shortwave radiation and the absorption and re-emission of longwave radiation due to clouds is key to analyzing the overall effect on the climate. As such, constraining the cloud optical depth is crucial.

1.4 The Phoenix Mars Mission

The Phoenix Mars Mission was a crucial mission for understanding the Martian water cycle, including the formation and behaviour of water-ice clouds (Smith et al., 2008). Landing on Mars at the end of local spring in 2008, the Phoenix lander operated for 151-sols in the northern polar region of the planet (68.2°N, 233°E). The Phoenix lander remains the most northern-based lander on Mars, as shown in Figure 1.6, giving it a unique ability to study the atmosphere of the Martian arctic from the surface.

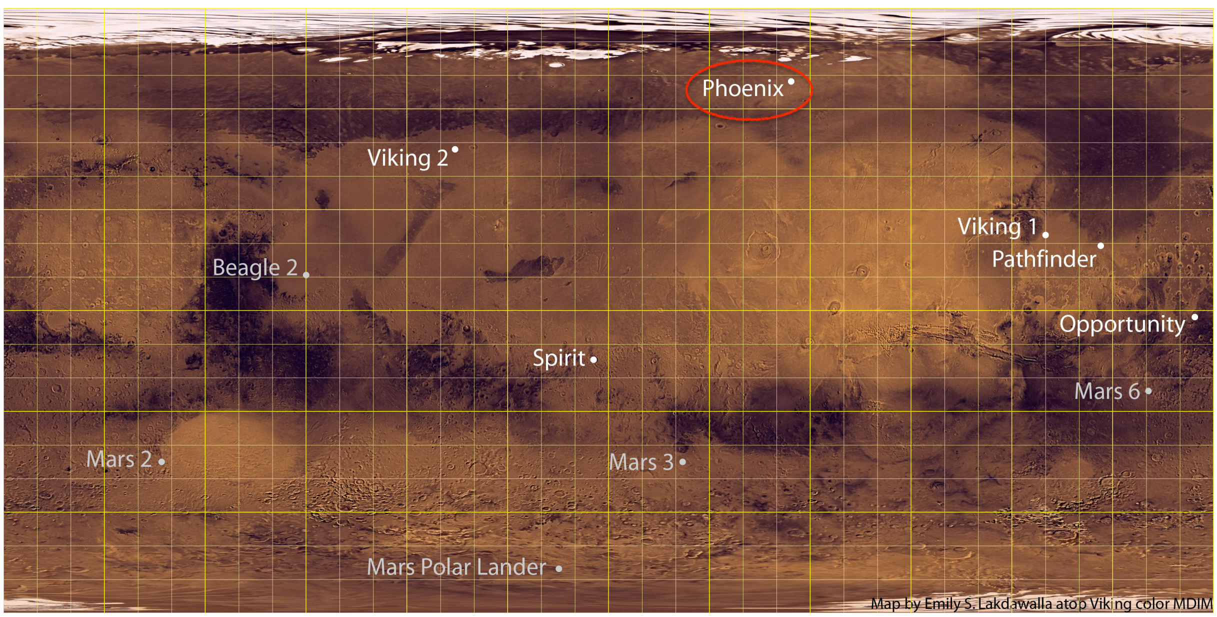

Figure 1.6: Map produced by Emily Lakdawalla, edited to include the red oval around the Phoenix landing site. The location of several landers and rovers on Mars can be seen, with the Phoenix lander at the highest northern latitude. The Phoenix lander's location allowed it to study the water-cycle in the north, including ground ice and water-ice clouds. Source: NASA / JPL-Caltech / USGS (image); Emily Lakdawalla (map)

The Phoenix lander was equipped with several instruments which were used to characterize local atmospheric properties. Namely, these instruments include the Surface Stereo Imager (SSI), the Phoenix light detecting and ranging (lidar) instrument, and the meteorological (MET) suite. These instruments are shown on the lander in Figure 1.7. The SSI was the main camera used for imaging the sky, taking several images per sol to characterize dust and cloud dynamics (Moores et al., 2010). The lidar worked by emitting laser light pulses into the atmosphere, measuring the backscatter as a function of time (Whiteway et al., 2008). The Phoenix lidar used a neodymium-doped yttrium aluminum garnet (Nd:YAG) laser, transmitting pulses at 532 nm. Lastly, the MET suite took near-continuous measurements of temperature and pressure at the landing site (Taylor et al., 2008). All instruments worked to monitor atmospheric conditions, including cloud, dust, and weather activities occurring throughout the mission.

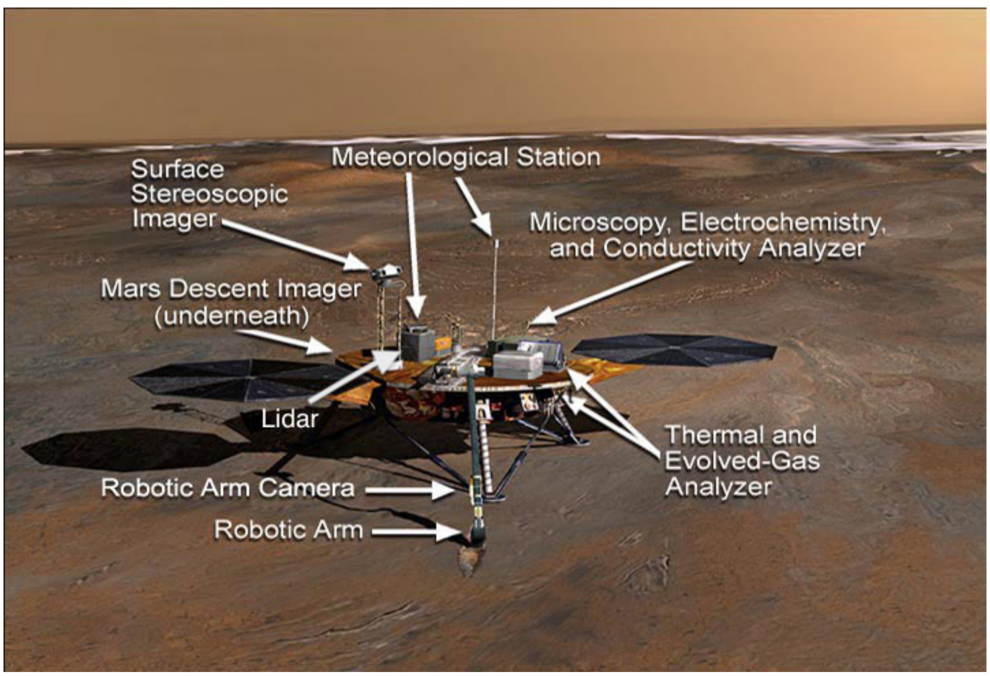

Figure 1.7: The Phoenix lander with labels showing the instruments used throughout the mission. Image credit: NASA/JPL-Caltech/UA/Lockheed Martin

Water-ice clouds were detected at the Phoenix site on several occasions. Dickinson et al. (2010) used the lidar several times per sol throughout the mission to stitch together diurnal and seasonal variabilities in the clouds. In the beginning of the mission, the lidar detected only dust distributed evenly throughout the PBL during the daytime (Komguem et al., 2013). However, nighttime use of the lidar after sol 38 saw sporadic water-ice fog and clouds (Dickinson et al., 2010). As the mission progressed, nighttime clouds were observed more frequently, with water-ice cloud properties after sol 60 shown in Figure 1.8. Nominally, water-ice clouds would form in the late evening, increasing in opacity throughout the night. As the air temperature warmed into the afternoon, the clouds would dissipate. This was demonstrated frequently in the latter two-thirds of the mission (Dickinson et al., 2010; Whiteway et al., 2009).

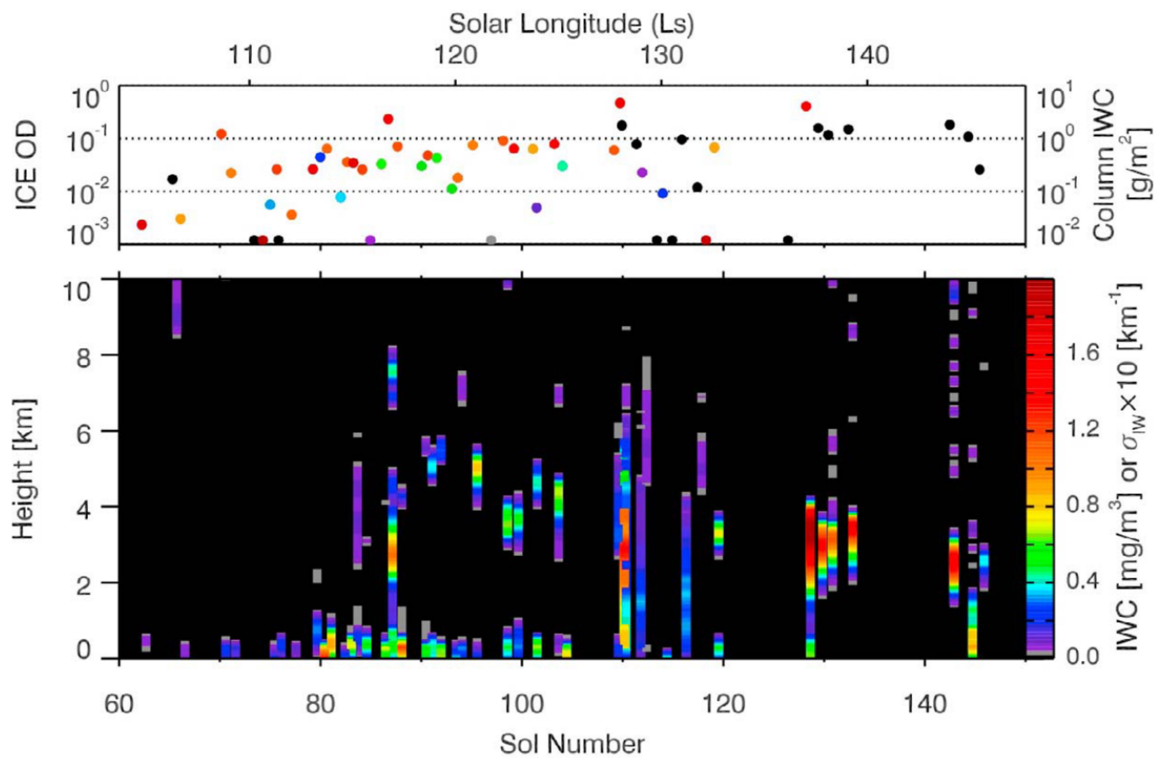

Figure 1.8: Figure from Dickinson et al., 2010, showing the sols on which the lidar detected water-ice clouds, and the corresponding altitudes above the landing site. The colour bar represents the ice-water content (IWC) of the clouds.

In addition to the repeatability of the cloud formation, properties of the clouds were found using the lidar. In the beginning of the mission when clouds were detected sporadically, they typically formed at 10 km in altitude (Whiteway et al., 2009), likely due to the colder temperatures higher in the atmosphere. As the mission continued, the clouds formed closer to the surface and up to 4 km in altitude. Because of the lower altitude of these clouds, it could be confirmed the clouds were composed of water-ice, as CO_2 could not condense at such altitudes due to the temperatures. Interestingly, on sols 99 and 109, Fall Streaks were observed falling from the clouds, and can be seen in Figure 1.9. Water-ice crystals were observed to precipitate from the clouds and sublimate in the air below the clouds – even falling all the way to the surface on sol 109 (Whiteway et al., 2009). In combination with the subsurface ice uncovered at the Phoenix site (Mellon et al., 2009), the lidar analysis gives interesting insight into the water-cycle at the Phoenix site.

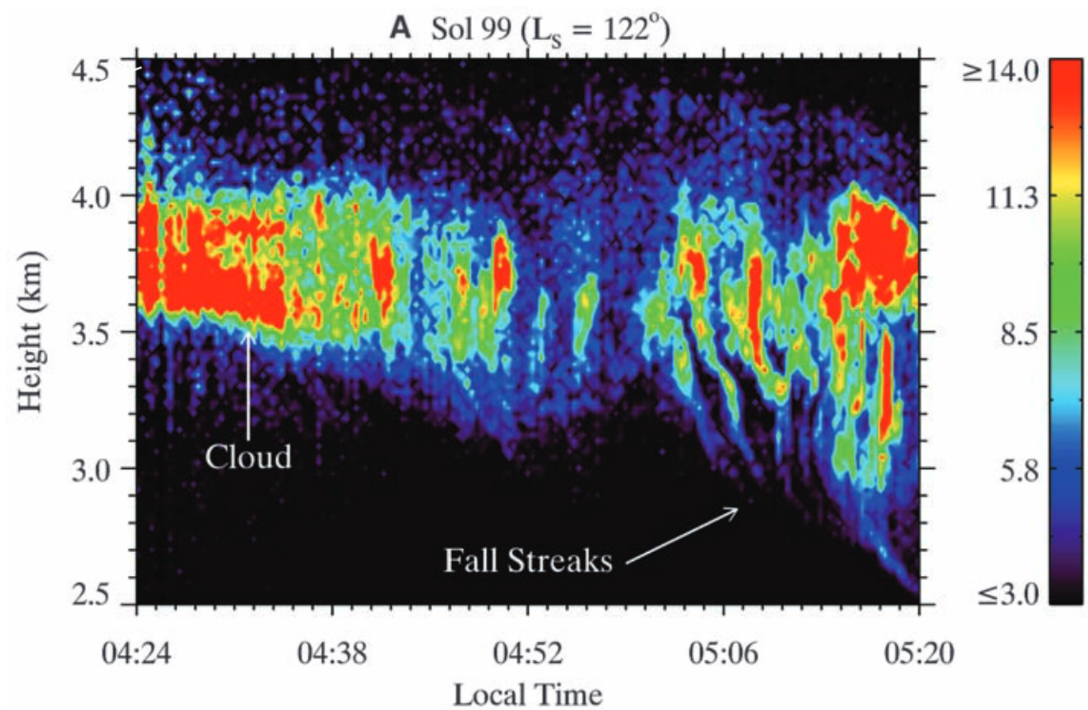

Figure 1.9: From (Whiteway et al., 2009), Fall Streaks were seen falling from the clouds in the early morning hours of sol 99. The water-ice particles precipitated from the cloud and sublimated in the air below. This was the first time precipitation was observed on Mars.

The SSI captured many images of clouds above the landing site throughout the mission, shown in Figure 1.10, giving insight into their morphology and microphysical properties. Two types of image sequences were taken to analyze atmospheric dynamics – Zenith movies (ZMs) and Supra-horizon movies (SHMs) (Moores et al., 2010). A ZM consists of several frames taken in succession of the sky with the SSI pointed at an elevation angle of 83.79°. SHMs are similar to ZMs, with a change in the elevation angle of the camera. SHMs are pointed just above the horizon to achieve the longest path length through the atmosphere (Moores et al., 2010). The movies were often imaged with both camera eyes, allowing a comparison between filters.

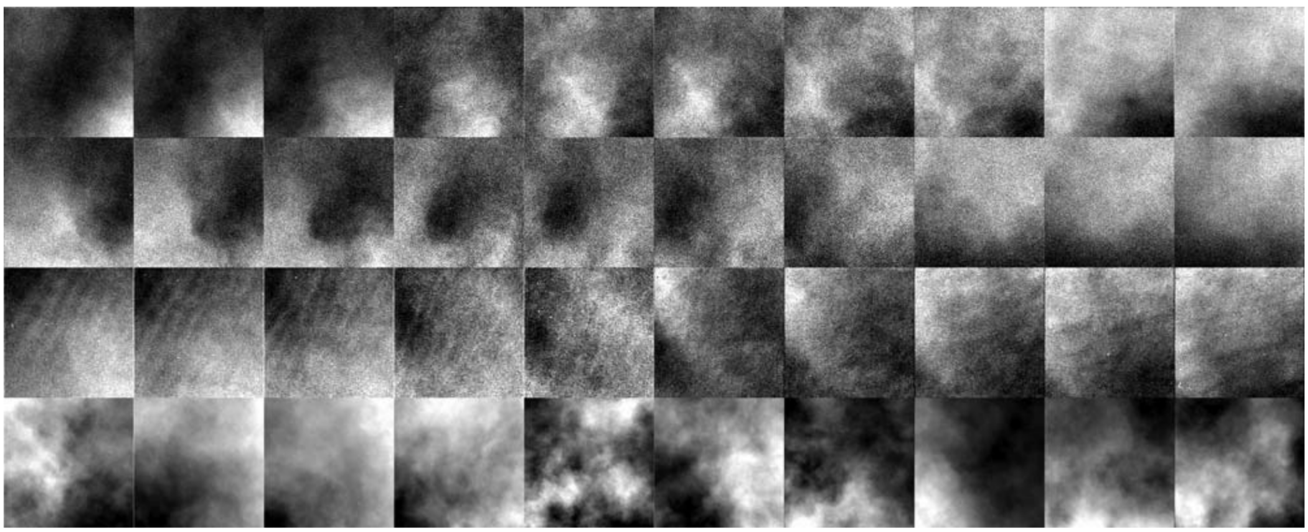

Figure 1.10: Moores et al. (2010) analyzed ZMs to characterize the atmospheric dynamics at the Phoenix site. Each row represents a single 10-frame ZM imaged in the right-eye blue filter. From top to bottom, these represent sol 8, sol 9, sol 101, and sol 141. Water-ice clouds above the Phoenix lander are seen on sol 101 and sol 141.

Several types of clouds were detected within the movies – from sub-optical, streaky clouds to thick, cumulus-like clouds. In some instances, clouds grew and dissipated within a single movie, showing very rapid, convective motion that is similar to terrestrial cumulus clouds (Moores et al., 2010). Additionally, a few movies saw multiple layers of clouds, moving in different directions at different altitudes. By imaging the lidar laser with the SSI, surface fog was observed on several occasions (Moores et al., 2011).

At the Phoenix landing site, the opacity of the atmosphere, including water-ice clouds, was found using the ZMs and SHMs acquired with the SSI (Moores et al., 2010). The movies were processed using a technique known as Mean Frame Subtraction (MFS). A "mean frame" is created where each pixel is the averaged radiance from the corresponding pixels in the individual movie frames (typically 10 frames per sequence). This "mean frame" is then subtracted from each individual frame, revealing movement within the images. Using MFS allowed Moores et al. (2010) to pull out a time-varying signal within the images, viewing clouds that would otherwise be too optically thin to observe by eye.

The calculation of the cloud optical depths involved using high and low radiance values in the images to discern between clouds and empty sky. This allowed for a calculation of the optical depth of the time-varying layer (Moores et al., 2010), however it is important to note that these calculations must be viewed in a relative sense only because the low radiance points in an image may not be an empty sky, but instead a very thin layer of clouds. Additionally, Moores et al. (2010) notes that enhanced dust loading in the beginning of the mission may increase the optical depth of the time-varying signal without an actual increase in water-ice optical depth. Constraining the water-ice optical depth throughout the mission would better characterize the Martian polar environment, especially in regards to the climatic effect of clouds.

While the lidar and SSI observed water-ice clouds many times throughout the mission, leading to a substantial increase in knowledge about water-ice clouds in the polar region of Mars, a problem remains: both instruments leave large temporal gaps in the cloud record due to operational constraints. The SSI imaged the sky for approximately 28 hours of the mission, covering only 0.76% of the entire mission (Moores et al., 2010). At its most optimal, the lidar ran 3 time per sol in 20 minute intervals, covering only 4% per sol. Additionally, the lidar was not run overnight until sol 38, where it detected fog for the first time (Dickinson et al., 2010). By the end of the mission, power constraints led to nighttime preclusion of the lidar. Any clouds forming throughout the night in the beginning and end of the mission

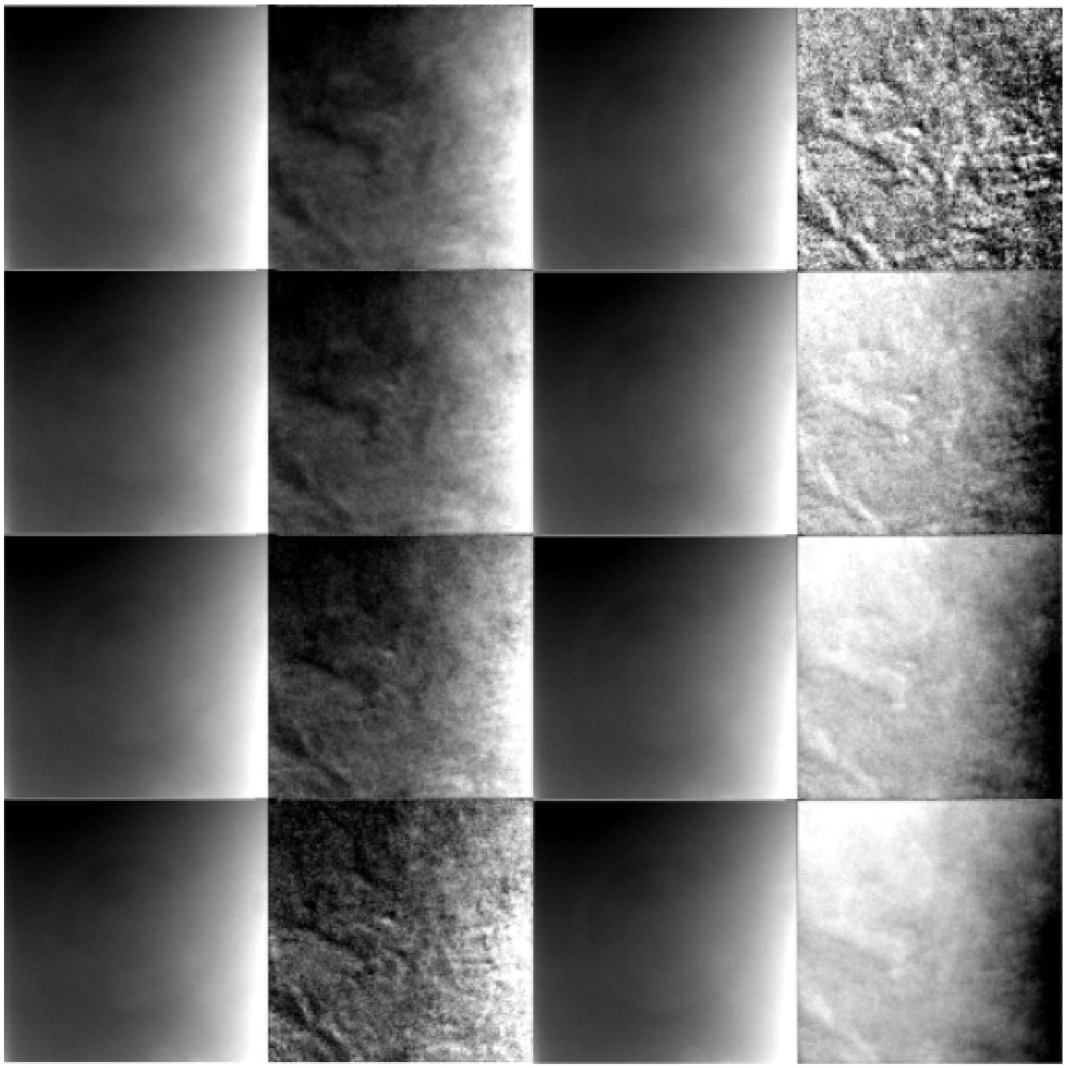

Figure 1.11: From (Moores et al., 2015). The first and third columns show ZMs taken in Gale Crater with MSL before MFS occurs, where clouds are difficult to spot in the image. The second and fourth column show the images after MFS is applied to the images, revealing a strong time-varying signal.

would be missed. Filling in these temporal gaps would help with determining the seasonal and diurnal variability of water-ice clouds throughout the entire mission.

In this work, we fill in temporal gaps in the cloud record by investigating whether water-ice clouds lead to similar temperature perturbations as seen in Gale Crater by Cooper et al. (2021). This is achieved by analyzing the data from the MET temperature sensor onboard

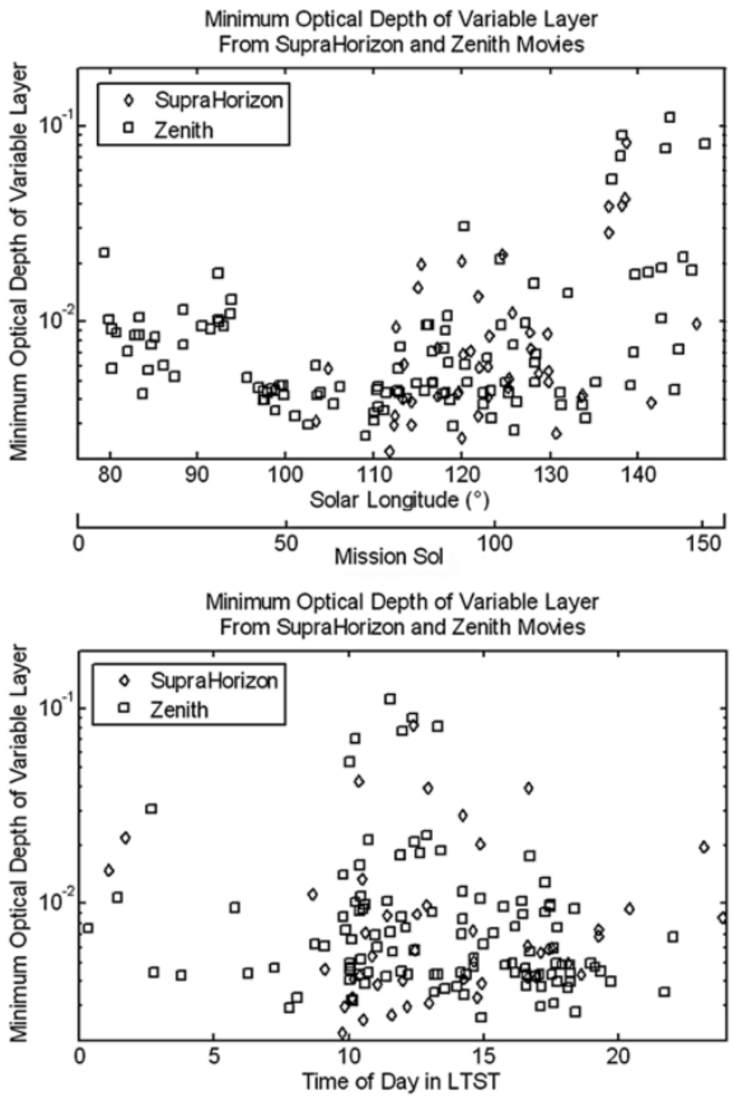

Figure 1.12: From (Moores et al., 2010). The optical depth of the time-varying layer as derived from the ZMs and SHMs is shown as a function of mission sol and time of day. Due to the methods used, the optical depths are to be viewed in a relative sense.

the Phoenix lander, which ran near-continuously the entire mission. By modelling the MET temperature with and without the radiative influence of clouds, a record of clouds can be built throughout the mission, filling in the gaps left by the lidar and SSI.

Additionally, to better constrain the optical depth of the water-ice clouds throughout the Phoenix mission, we will use both the images taken by the SSI and a radiative transfer model to derive the cloud opacities. Clouds particles can be added into the radiative transfer model in several wavelengths until the radiances given by the model match the radiances seen in the SSI image. This removes the assumption in Moores et al. (2010) that the low radiance points are empty sky, better constraining the values of optical depth throughout the mission.

1.5 Motivation and Organization of Thesis

This works seeks to characterize water-ice clouds at the Phoenix mission landing site. This is achieved by investigating their opacities throughout the mission from radiative transfer in thermal and visible wavelengths. Firstly, Chapter 2 will describe the methods used to create a record of water-ice clouds by modelling the temperature data collected by the 2 m MET sensor. This record of clouds will fill in temporal gaps left by the lidar and SSI. The results in Chapter 2 will explore the following questions:

1. What are the seasonal and diurnal variabilities in the cloud emission at the Phoenix landing site?
2. What effect do the clouds produce on the near-surface temperature?
3. What is the relationship between the lidar-derived water-ice optical depth and cloud emission?

In chapter 3, we will use a radiative transfer model to measure the visible opacity of the clouds imaged by the SSI. This work seeks to build on the work by Moores et al. (2010), constraining the optical depths of the observed clouds to better understand their potential effects on the climate. This work will seek to answer the following questions:

1. What is the diurnal and seasonal variability of the cloud opacity?

2. Does the radiative transfer method better constrain the opacity compared to the MFS method used by Moores et al. (2010)?

Finally, Chapters 4 and 5 will discuss the conclusions of this work and potential future work brought about by these analyses, respectively.

Chapter 2

A Record of Water-Ice Clouds at the Phoenix Landing Site Derived from Modelling MET Temperature Data

2.1 Author Contributions

This research was a collaboration between Grace Bischof, Brittney A. Cooper, and John E. Moores, who proposed the study concept. The implementation of the methods, analysis and interpretation of the data, and writing were carried out by Grace Bischof. All authors contributed to the revision of this work.

2.2 Methods

2.2.1 Phoenix MET suite

Along with the lidar and SSI, Phoenix carried a MET instrument suite to monitor the local meteorological conditions of the colloquially named Green Valley area of the Martian Arctic (68.2°N, 233°E), 20 km from Heimdal crater. The MET suite included three fine-wire thermocouple temperature sensors located 1 m, 0.5 m, and 0.25 m vertically from the deck of the lander, itself 1 m from the surface (Taylor et al., 2008). The absolute accuracy of the temperature sensors was ±1 K with a resolution of 0.5 K (Taylor et al., 2008). The temperature was measured throughout each sol, with data taken at a frequency of 0.5 Hz. A nominal 20-minute break per sol occurred around midday for data transfer purposes. In addition to the temperature sensors, the Phoenix lander carried a tell-tale wind indicator to study the speed and direction of wind (Gunnlaugsson et al., 2008), and a pressure sensor to monitor the near-surface pressure (Taylor et al., 2008).

An analysis into the temperature data throughout the mission by Davy et al. (2010) shows the temperature sensor closest to the lander was affected by the heater on the lander (Davy et al., 2010). As a result, this work uses only the data from the sensor furthest from the lander (1 m) to reduce any heat contamination in the data.

High-resolution reduced data records (RDRs) are used for this work, obtained from the Planetary Data System (PDS): Atmospheres Node. Each RDR counts time in seconds from the start time of the instrument in Earth seconds, and temperature is reported in Kelvin (K). An RDR was downloaded for each sol of the mission where available.

2.2.2 Surface Energy Balance

The focus of this work is to build a record of clouds by modelling the MET temperature data and analyzing the radiative flux received at the surface due to clouds. As such, an energy balance equation is required for the modelling and analysis. The energy balance is adapted from Martínez et al. (2014) and given by

$$G = S(1-\alpha) + LW_{\downarrow} - LW_{\uparrow} - H - LE + R \tag{2.1}$$

where G is the net flux into the ground, S is the solar flux at the surface minus a portion reflected to space dependent on the surface albedo, α. $LW_{\downarrow}$ represents the longwave flux emitted from atmospheric gases and dust only, while $LW_{\uparrow}$ represents longwave flux emitted from the surface. H is the sensible heat flux, which describes the energy exchange between the surface and near-surface atmosphere. LE is the latent heat as water changes phase between subsurface ice and water vapour. However, the latent heat flux, described in Martinez et al. (2014), is on order of 1 W m^{-2} and is neglected in this analysis. The last term, R, represents the thermal flux emitted by the clouds. Because clouds absorb some of the longwave flux given off from the surface, then re-emit a fraction of the flux back toward the ground, we refer to R as "cloud emission" throughout this work as a shorthand. A description of the parameters is found in Table 2.1.

The solar flux incident at the Phoenix lander is based on a model developed by Vicente-Retortillo et al. (2015). Equation 1 from Vicente-Retortillo et al. (2015) takes into account the solar longitude of Mars, obliquity of Mars (25.2°), distance from the sun, and latitude of the Phoenix lander (Vicente-Retortillo et al., 2015). Martian dust scatters visible-band solar radiation, therefore the single scattering albedo and asymmetry factor of dust are incorporated into Equations 10-23 of this model, and are set to 0.97 and 0.70, respectively (Vicente-Retortillo et al., 2015). Dust optical depths for each sol of the mission are from

Tamppari et al. (2010), where a higher dust abundance is noted at the landing site during the year Phoenix operated compared to other Mars Years (Tamppari et al., 2010). The visible-band surface albedo is set to $\alpha = 0.18$, consistent with measurements of the Green Valley area by the Mars Global Surveyor, which makes measurements in the 0.3 to 2.7 μm wavelength range (Savijärvi and Määttänen, 2010).

Table 2.1: Nomenclature table for model variables

Parameter	Description	Unit
T_g	Surface temperature	K
T_a	Air temperature at 2m	K
S	Solar flux	W m^{-2}
G	Net flux into at surface	W m^{-2}
$LW_{\downarrow}$	Downwelling longwave flux	W m^{-2}
$LW_{\uparrow}$	Upwelling longwave flux	W m^{-2}
H	Sensible heat flux	W m^{-2}
R	Flux emitted from clouds	W m^{-2}

The downwelling longwave flux is modelled in a simplified manner described in Savijärvi (2014). The downwelling flux is dependent on the air temperature, emission of longwave radiation from CO_2 in the 15 μm band, and opacity of dust (Savijärvi, 2014). The upwelling longwave flux from the surface is calculated by

$$LW_{\uparrow} = \epsilon \sigma_B T_g^4 \tag{2.2}$$

where ϵ is the surface emissivity and is set to 0.96 derived from Mars-analogue laboratory experiments and data acquired at the Opportunity landing site (Christensen et al., 2004), σ_B is the Stefan-Boltzmann constant, and T_g is the ground temperature.

The sensible heat flux typically gives a small contribution to the surface energy balance. The sensible heat flux is introduced into the model as a correction factor on G, adjusted so the values are consistent with the flux values derived at the Phoenix site under stable conditions (Davy et al., 2010). This method is in excellent agreement with Davy et al. (2010) overnight but does underestimate the sensible heat flux during the day when the dynamical conditions near the surface are unstable.

The cloud emission, R, is an independent parameter in our model. R is calculated at 2-hour intervals, with the first interval beginning at 12:00 to 14:00 Local True Solar Time (LTST). Because the model becomes unstable when large flux values are input at once, the flux values are gradually ramped up. While clouds can form on much shorter timescales than 2 hours (Moores et al., 2010), the input of R appears immediately in the air temperature. This immediate change in temperature is likely not reflective of the Martian environment, as there would be some thermal timescale over which the effect of the cloud becomes important. Using 2-hour time increments for the clouds allows the change in the temperature to happen gradually, rather than instantly.

Unlike the study from Cooper et al. (2021) where ground and air temperatures are recorded by instruments aboard Curiosity and both temperatures are used in their analysis, Phoenix did not carry a ground temperature sensor. Because of this, the surface energy balance is used as input to model the subsurface heat conduction at the Phoenix landing site to estimate ground temperature. This model is adapted from Schörghofer (2020), where the model's upper boundary condition involves the incoming solar and atmospheric flux terms. The equation governing the heat conduction is given by:

$$\rho c \frac{\partial T_g}{\partial t} = \frac{\partial}{\partial z}\left(\kappa \frac{\partial T_g}{\partial z}\right) \tag{2.3}$$

where ρ is the density of the regolith, c is the heat capacity at constant pressure, κ is the thermal conductivity, z is the depth, and t is time (Schörghofer 2020).

The thermal inertia of the soil, I, is related to ρc and κ by:

$$I = \sqrt{\rho c \kappa} \tag{2.4}$$

Thermal inertia is an important factor for determining the ability of the surface to exchange energy with the subsurface (Martínez et al., 2014). A subsurface composed of a low thermal inertia material will exchange energy more readily with the surface, resulting in higher diurnal amplitudes in the surface temperature. Alternatively, high thermal inertia suppresses the diurnal amplitude (Mellon et al., 2000). At the Phoenix site, the TECP measured the thermal properties of the regolith (Zent et al., 2010). For this work, a fixed thermal inertia of 295 J m^{-2} $s^{-\frac{1}{2}}$ K^{-1} is used, consistent with measurements from Zent et al. (2010).

Subsurface ice was discovered at the Phoenix site using the Robotic Arm (Mellon et al., 2009). The ice is incorporated into the conduction model by making the depth grid a 2-layered grid, with ice beginning at 10.4 cm. While the average depth of ice was found to be 4.6 cm, depth values less than 10 cm resulted in modelled temperatures that were low as the heat was radiated away too quickly. Ice was found down to 14 cm (Mellon et al., 2009), meaning the depth of 10.4 cm used in the model is not an unreasonable choice. The ice is assigned a thermal inertial of 1274 J m^{-2} $s^{-\frac{1}{2}}$ K^{-1} (Schorghofer, 2005).

Once the ground temperature is found by the energy balance and subsurface conduction scheme, the air temperature is solved for at each time step. The ground and air temperature are related to the sensible heat flux by:

$$H = k^2 c_p u \rho_a f(R_b) \frac{T_g - T_a}{ln^2\left(\frac{z_a}{z_0}\right)} \tag{2.5}$$

where k is the Von Karman constant and is equal to 0.4, c_p is the constant pressure specific heat of CO_2 equal to 736 J kg^{-1} K^{-1}, u is the wind speed at the landing site retrieved from (Holstein-Rathlou et al., 2010), $\rho_a = 0.02$ kg m^{-3} is the density of the air at 2 m, $f(R_b)$ is a thermal stability term related to the Bulk Richardson number described in Savijärvi & Määttänen (2010). The air temperature at 2 m is given by T_a. The surface roughness, z_a, is set to 0.6 cm (Holstein-Rathlou et al., 2010), and the height above the ground, z_0, is 2 m. Values for these constants can be found in Table 2.2.

Table 2.2: Nomenclature table for model constants

Symbol	Description	Value	Reference
α	Visible band surface albedo	0.18	(1)
ϵ	Surface emissivity	0.96	(2)
σ_B	Stefan-Bolztmann constant	5.67 x 10^{-8} W m^{-2} K^{-4}	N/A
I	Thermal intertia of ground (ice)	295 (1274) J m^{-2} s$^{-\frac{1}{2}}$ K^{-1}	(3),(4)
ρc	volumetric heat capacity of ground (ice)	1.3 x 10^6 (6.5 x 10^5) J K^{-1} m^{-3}	(3),(4)
κ	thermal conductivity of ground (ice)	0.66 (2.5) W m^{-1} K^{-1}	(3), (4)
k	Von Karman constant	0.4	(5)
c_p	Constant pressure specific heat capacity of CO_2	736 J kg^{-1} K^{-1}	(5)
ρ_a	Density of air at 2 m	0.02 kg m^{-3}	(5)
z_a	Surface roughness	0.06 m	(6)
z_0	Height above surface	2 m	N/A
u	Wind speed	4-6 m s^{-1}	(6)

(1) Savijärvi & Määttänen (2010); (2) Christensen et al. (2009); (3) Zent et al. (2010); (4) Schorghofer et al. (2005); (5) Mártinez et al. (2014); (6) Holstein-Rathlou et al. (2010)

The modelled air temperature, run with a timestep of 120 s, is plotted against the temperature data recorded from the MET instrument, with the MET data filtered to select a data point every 120 s. If the modelled temperature and the measured MET temperature are equal, R remains zero over the entire run of the model. If the temperatures are not the same, R is varied as needed to match the modelled temperature to the MET data recorded in-situ. Although the temperature model runs for an entire diurnal cycle, cloud emission is only considered between the hours of 22:00 and 10:00 LTST. The Martian atmosphere has been shown to have a superadiabatic layer near the surface during the day (Smith et al., 2006). Convection will be important for the transport of heat during the day, which is not considered in this model. In the hours after 22:00, the atmosphere has become much more stable, meaning radiation is the main driver of the temperature, and cloud emission has a noticeable effect on the temperature.

The analysis to derive R is completed for every sol of the mission for which MET data are available. A few sols – sol 26, 27, and 28, for example – are not included due to a lack of MET data. Some sols had only a few hours of coverage, so a full diurnal record could not be determined. In general, the MET data were arranged to run from noon-to-noon LTST for each sol, or from the least cloudy part of the day, through the cloudiest to the least cloudy part of the next day. This has the benefit of eliminating any edge inconsistencies in the model.

2.3 Results

The left panels of Figure 2.1 (panels a, d, and g) show the modelled diurnal atmospheric temperature for sols 9-10 (Fig 2.1a), 64-65 (Fig 2.1d), and 137-138 (Fig. 2.1g) as function of LTST, with and without R in the energy balance equation. These sols have L_s values of 80.48°, 105.04°, and 141.30°, respectively, and were selected to show a range in R-values derived from the model, displayed in the right panels of Figure 2.1 (panels c, f, and i). The middle panels of Figure 2.1 (panels b, e, and h) display the flux values from the energy balance equation (Equation 2.1).

On sol 9-10, as shown in Figure 2.1c, the value for the cloud emission, R, remains zero over the entire run of the model and no clouds need be present in order to explain the temperature profile. The daytime and nighttime temperatures fit the MET data well without additional flux needed to warm the near-surface, seen in Figure 2.1a. On sol 64-65, R begins increasing at 2:00 LTST on the morning of sol 65, reaching 10 W m^{-2} by 4:00. The cloud emission remains constant until 6:00, falling back to zero by 8:00. The cloud emission begins to rise

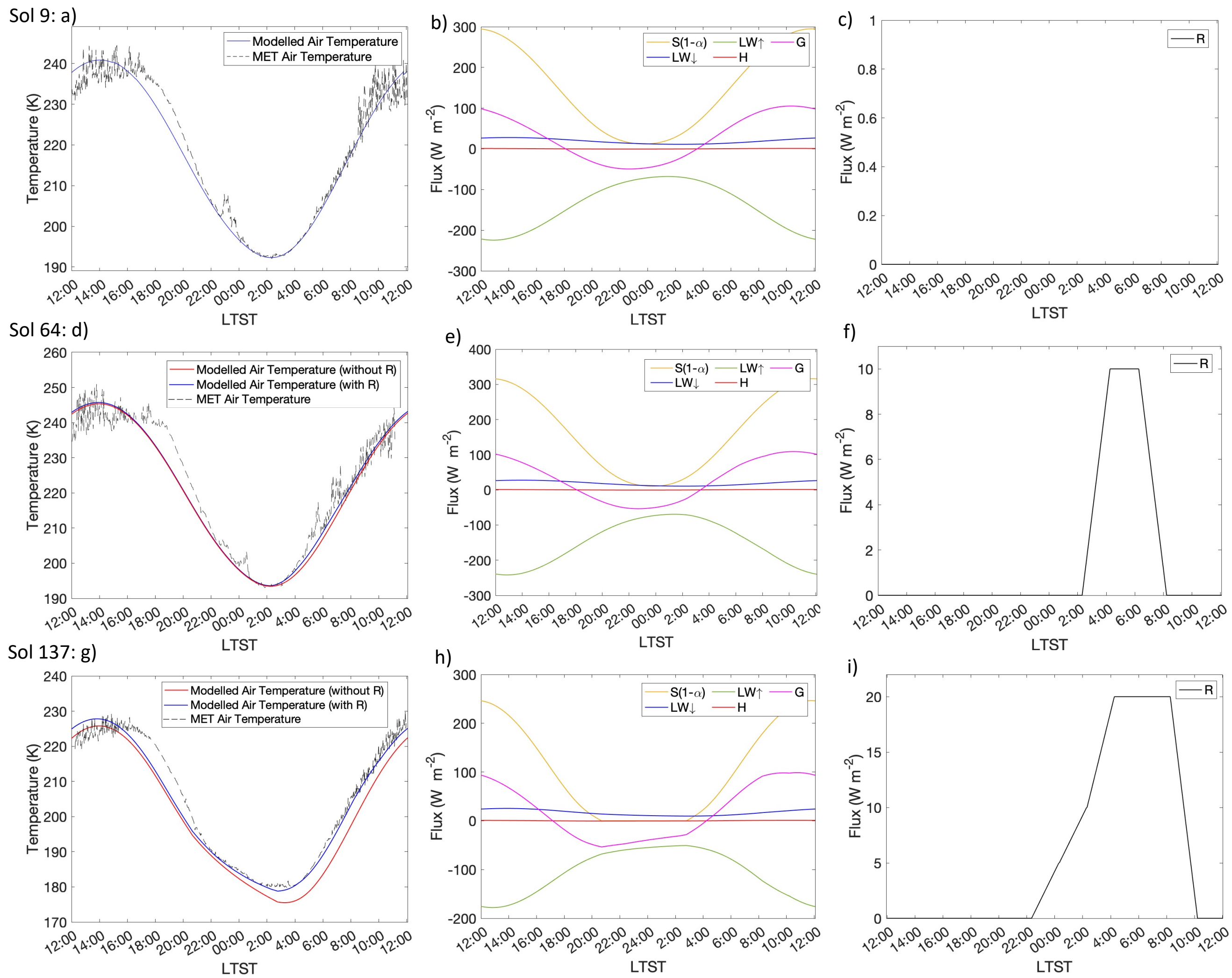

Figure 2.1: Diurnal atmospheric temperature at a height of 2 m above the surface on (a) sol 9 ($L_s = 80.48°$), (d) sol 64 (L_s=105.04°), and (g) sol 137 ($L_s = 141.31°$). The red line shows the modelled temperature with no cloud emission in the energy balance equation, meanwhile the blue line is the modelled temperature when cloud emission is included in the energy balance equation. The grey line is the data collected by the highest temperature sensor of the MET instrument. The first 5 terms of Equation 1 are shown in (b, e, h). Panels (c, f, i) are the values of R found by the model for the selected sols. Note the scale difference on the y-axis between panels (b,e,h) and (c,f,i). These 3 selected sols represent a range of derived R-values used in the modelling, with the top panels (a,b,c) showing a day when emission from clouds is zero, the middle panels (d,e,f) showing a day when the effect is small, and the bottom panels (g,h,i) showing a day with a considerable amount of emission over a long time period.

earlier on sol 137, starting at 22:00. R increases at a consistent rate until its maximum of 20 W m^{-2} at 4:00. The flux begins decreasing at 8:00 and is back to zero by 10:00 on the morning of sol 138. A reduced chi-square goodness-of-fit test was carried out to determine if the MET data are well-described by the temperature model. Each sol has a goodness of fit probability greater than 0.9, where any number larger than 0.1 is considered an excellent fit (Press et al., 1992).

With the values of R introduced to the model, the modelled air temperatures match well to the MET data, as shown in Figure 2.1 (panels d and g), between 22:00 and 10:00 LTST. As mentioned in Section 2.2, the cloud emission is not considered outside of these times. Figure 2.1 shows the temperature cycles rapidly during the day, evidence for the convective nature of the daytime atmosphere. Another discrepancy is seen in nearly every sol, where the modelled temperature begins to decrease earlier in the afternoon compared to the MET data. It has been suggested that perchlorates at the Phoenix site may have a hydration phase transition at the conditions seen by the MET and TECP (Chevrier et al., 2009; Nikolakakos and Whiteway, 2015). Latent heat from perchlorate transition may cause a portion of the temperature difference seen between the MET data and temperature model, as this extra heating was not included in the model, although it is unlikely that the phase transition is the sole factor. Nevertheless, the discrepancy does not occur at a particularly cloudy time of the day and the phase transition is largely restricted to the period around sunset.

The solar flux and outgoing longwave flux are the dominant energy terms, as seen in Figure 2.1, panels b, e, and h. Phoenix's northern location meant the sun did not set until sol 86 of the mission, as seen on sols 9 and 64, resulting in a non-zero solar flux term for these sols. The diurnal solar flux is at its peak around sol 64, shortly after the northern summer solstice. By sol 137, the sun sets between 22:00 and 3:00. The atmospheric downwelling longwave flux remains fairly consistent over the 3 sols shown, with nighttime values around 20 W m^{-2}. On a diurnal basis, changes in $LW_{\downarrow}$ are due to the changing atmospheric temperature, the dominant term in the equation for the downwelling longwave radiation. On sol 137, the flux emitted from clouds is larger than the downwelling flux from dust and atmospheric gases.

As noted in Section 2.1, the sensible heat flux is an important factor in the modelling, linking the ground temperature to the air temperature. During the day when conditions are dynamically unstable, the model underestimates the sensible heat flux. Davy et al. (2010) reports fluctuating daytime values, which average around 4 W m^{-2}, meanwhile the model gives values around 1.5 W m^{-2}. This results in daytime temperature modelling slightly higher than observed during the mission. At night, the modelled sensible heat flux agrees closely to the numbers calculated by Davy et al. (2010). The sensible heat flux at nighttime typically dropped to values around -0.5 W m^{-2}.

To analyze the radiative effect the clouds had over the entire duration of the mission, the cloud emission as a function of time is plotted for each sol, shown in Figure 2.2a. At the beginning of the mission, lower amounts of cloud emission are modelled throughout the night – often around 5 W m^{-2}, but occasionally reaching 10 W m^{-2}. The cloud emission is shown to begin no earlier than 22:00 and end no later than 10:00 LTST. This build-up and decay of longwave flux demonstrates the formation and dissipation of clouds in the atmosphere. A few sols do not show any cloud emission whatsoever, indicating there were no clouds to re-radiate longwave radiation back toward the surface.

Near the middle of the mission, from sol 55 to 80, the amount of cloud emission is smaller than in the earlier and later parts of the mission. Several nights have no cloud emission whatsoever. In this time, R frequently becomes positive after 02:00 and disappears by 8:00, with similar emission patterns to the beginning of the mission, but more variable. Shown in Figure 2.2b, this is the time of the mission just past summer solstice. At this time of the year, Phoenix sees the warmest overnight temperatures, and, from Figure 2.2a, the onset of clouds tends to overlap with the coldest part of the night.

Between sol 90 and 150, the cloud emission reaches its maximum. Many sols have an R

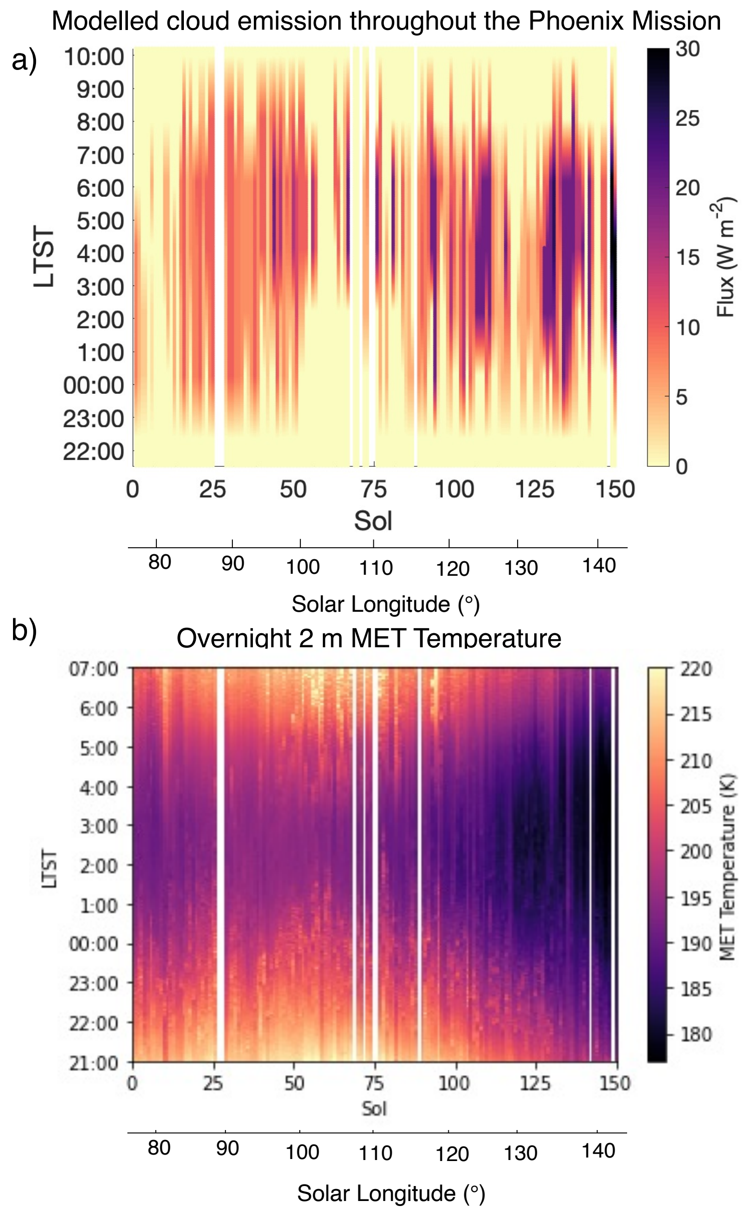

Figure 2.2: (a) Cloud emission as a function of time plotted for each mission sol and solar longitude. Summer solstice occurs at $L_s = 90°$. A near continuous record of water-ice clouds is built by examining the longwave flux emitted from clouds. The cloud emission typically begins in the night and ends in the late morning, indicating the formation and dissipation of clouds. (b) Overnight MET temperature taken from the sensor 2 m above the surface. The peak in cloud emission corresponds to the time during the mission when the overnight temperatures are lowest.

value near or greater than 20 W m^{-2}, usually occurring between 2:00 and 6:00. In Figure 2.2b, the coldest nightly temperatures occur near the end of the mission, corresponding to the peak in cloudiness. A slight dip in R is seen between sols 120 and 127, where maximum values were around 5 W m^{-2}.

Longwave flux emitted by the clouds towards the surface causes an increase in the surface and near-surface temperature. Figure 2.3a demonstrates the maximum change in temperature for each sol found by taking the the difference in temperature when the model is run with $R = 0$ for the entire run, versus when the model is run with flux values from Figure 2.2a. The clouds provide a warming of less than 4 K for the majority of sols, typically between 1-3 K. Toward the end of the mission, the thermal effect is larger, with the highest warming reaching 8 K. A large increase in temperature would require 30 W m^{-2} of flux emitted from clouds to reach the surface.

The net radiative flux, G, is integrated in Figure 2.3b, showing the total energy per square metre at the surface for each sol of the mission. The subtle curve shows the total energy balance is driven by seasonal effects, as the incoming solar flux and outgoing longwave flux are the dominant energy terms and have a seasonal dependence. Note that the period with the lowest cloudiness corresponds to the highest integrated flux during the mission. Figure 2.3c shows the integrated R-term for each sol. The integrated flux emitted from clouds contributes only a fraction of the total energy in the energy balance, shown by the difference in the y-axis on Figures 2.3b and 2.3c. Compared to the total energy balance, the cloud emission is also highly variable. This sol-to-sol variability suggests that clouds, and therefore the flux they emit, are driven by short-scale effects.

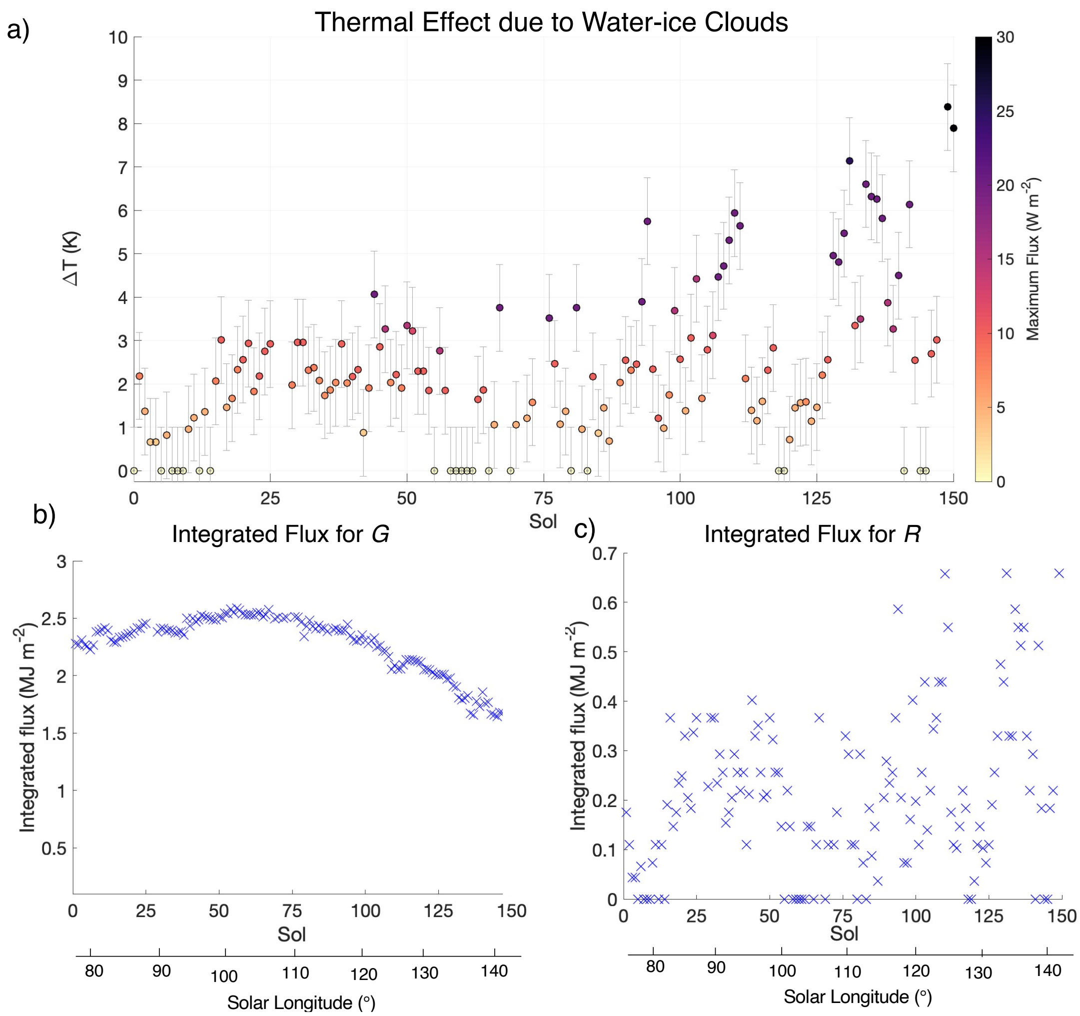

Figure 2.3: (a) The maximum amount of warming at the Phoenix site as a result of the flux emitted from the clouds. Error bars are given as ± 1 K, consistent with the uncertainty in the MET instrument. The warming is usually small, with values between 1-3 K. High R-values toward the end of the mission increase the warming up to 8 K. (b) The net flux, G, integrated throughout the mission. The net energy balance is driven by seasonal effects. (c) Integrated flux for the R-term only. The high variability indicates clouds are driven by small-scale effects.

2.4 Discussion

2.4.1 Cloud Emission and Water-ice Optical Depth

Commonly after sol 60, the lidar obtained data on the ice-water content (IWC) above the lander and the water-ice optical depth of the clouds was derived (Dickinson et al., 2010), shown in Figure 1.8. To investigate the radiative properties of water-ice clouds, we analyze the cloud emission with respect to water-ice optical depth retrieved by the lidar. This is shown in Figure 2.4. There were some instances where the lidar recorded a non-zero optical depth, meanwhile the temperature model did not show any cloud emission during that same period. For these instances we assume that the lidar, which points directly overhead, was taking measurements of an isolated cloud, rather than a cloud deck. Clouds at the Phoenix site were seen to change quickly, with optical depth changing rapidly (Moores et al., 2010). In such cases, the radiative impact of a rapidly changing, isolated cloud would be low, allowing these points to be removed. Uncertainty in the model is discussed further in section 2.4.2.

The contour lines in Figure 2.4 represent the temperature at which the cloud is radiating energy. The cloud emission, optical depth, and cloud temperature are related by

$$R = \left(1 - e^{-\tau}\right) \sigma_B T_c^4 \tag{2.6}$$

where τ is the optical depth of the clouds and T_c is the temperature of the clouds.

Figure 2.4 shows that optically thicker clouds tend to radiate more energy toward the surface, with most clouds having temperatures around 200 K, consistent with estimates from Whiteway et al. (2009). The highest temperatures observed, around 350 K, are not reflective of the Martian atmosphere, however this temperature is mostly observed as the upper limit to the uncertainty in the derived data points. There are cases where clouds with lower optical depths have a high cloud emission, which may be resolved by the range in error bars, but also points to potential complicated cloud microphysics. Terrestrial studies exemplify the challenge of modelling the infrared radiative properties of cirrus clouds, particularly when it comes to ice-crystal shape. When IWC is kept constant, a cloud composed of aggregates emits more radiation toward the surface than a cloud composed of spherical particles (Wendisch et al., 2007). The microphysics of cloud formation on Mars is still widely unknown, meaning

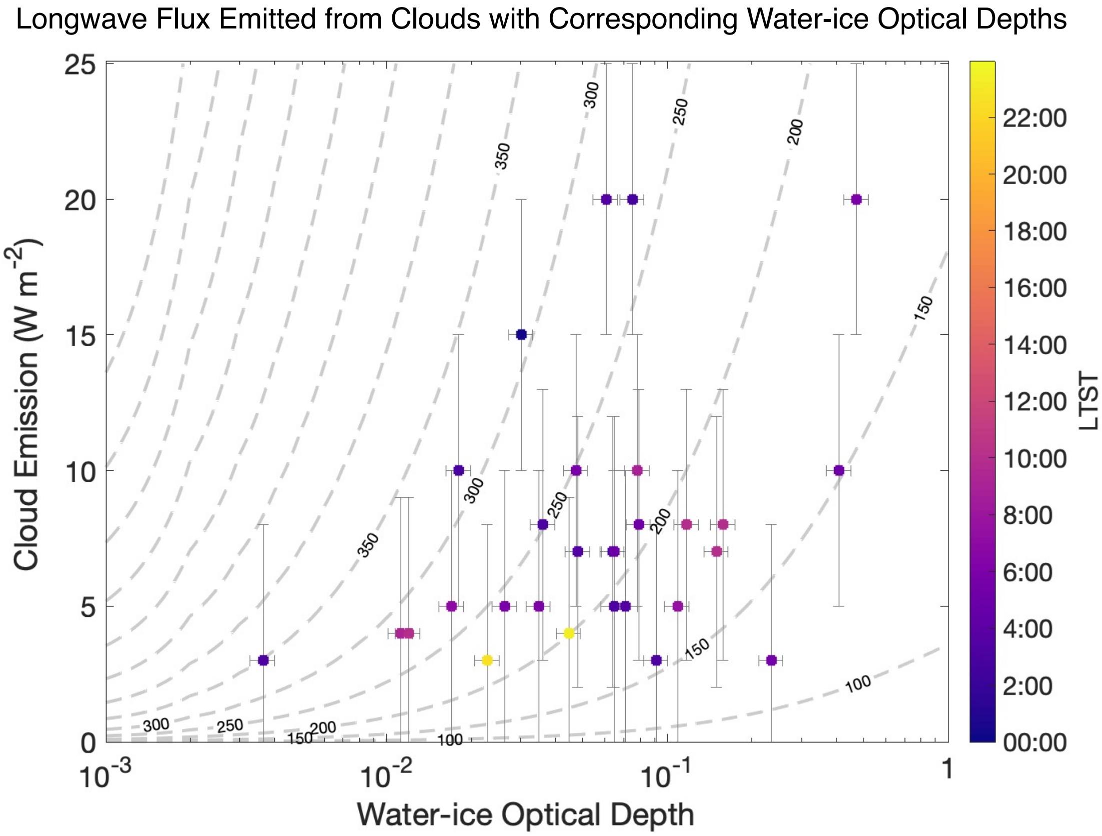

Figure 2.4: Cloud emission derived by the model as a function of water-ice optical depth retrieved from lidar data from (Dickinson et al. 2010). Dashed grey lines represent the temperature of the water-ice cloud emitting the longwave flux to the surface. Horizontal error bars represent an uncertainty of ±10%, cited by Dickinson et al. (2010). The MET temperature sensor has a cited error of ±1 K (Taylor et al. 2008). Since it takes about 5 W m^{-2} to increase the temperature by 1 K in the model, vertical error bars are given as ±5 W m^{-2}. This figure shows optically thicker clouds tend to radiate more energy toward the surface, while optically thin clouds radiate less.

ice-crystal type is not well understood (Cooper et al., 2020). This gap in cloud microphysics may explain why clouds with similar optical depths will radiate different amounts of longwave flux to the surface, potentially dependent on ice-crystal shape.

The points in Figure 2.4 showing the highest cloud emission were observed between 4:00 and 6:00 LTST, just past the coolest time of each night. Meanwhile, around 22:00, the optical depths and cloud emission are low, with warmer nighttime temperatures. This validates the idea from Figure 2.2a that clouds become optically thicker throughout the night, resulting in more cloud emission at the surface in the early morning hours.

An additional analysis is carried out, where a simple scattering model in a gray atmosphere is used to fit the results from the cloud emission and lidar analysis. The fraction of upwelling longwave flux "reflected" back toward the surface by water-ice clouds is given by

$$\frac{R}{LW_{\uparrow}} = \frac{(1-f)\tau}{1+(1-f)\tau} \tag{2.7}$$

where f is the degree to which clouds are forward scattering (i.e. a value of $f = 1$ indicates the clouds are completely forward scattering, while a value of $f = 0$ indicates the clouds are completely backscattering).

The model best fits the data with a value of $f = 0.36$, which has a R^2 coefficient of determination value of 0.397. This value of f suggests water-ice particles are slightly backscattering in thermal wavelengths. However, water-ice particles are often assumed to be isotropic. In such a case, with f = 0.50, the R^2 coefficient of determination is 0.298. Assuming isotropic particles yields a worse fit than the backscattering case, but it is a reasonable way to describe the data within error. It is important to note that this is a very simplified model to describe the interaction between the clouds and thermal radiation.

Interestingly, Figure 2.2a suggests clouds were present at the Phoenix site before they were observed by either the lidar or the SSI. At the beginning of the mission, the lidar operated solely during the day, so nighttime formation of clouds would have been missed. Moores et al. (2010) analyzed the minimum optical depth of the variable layer, which includes both dust and clouds, throughout the mission. Higher optical depth values were observed near the beginning of the mission, but it was noted that the higher optical depths might be explained by a higher dust abundance and did not necessarily indicate the presence of water-ice clouds. Although undetected by the lidar and SSI, it is not unreasonable to assume clouds may have formed at the beginning of the mission. Figure 2.2b shows nighttime temperatures in the first ~15 sols were cool and comparable to the nighttime temperature around sol 100, when clouds were certainly present. Water-ice retrievals from the Thermal Emission Spectrometer on Mars Global Surveyor in the northern polar region showed sporadic clouds with low optical depths in the late spring (Tamppari et al., 2008), corresponding to the time our work first sees cloud emission in the model. It is important to note that these clouds were observed between 12:30 and 14:30, and so are not the same clouds resulting in the cloud emission in Figure 2.2a. However, it is likely the afternoons were less cloudy than the nighttime (Tamppari et al., 2008), meaning the sporadic, positive detection of clouds in the afternoon suggest clouds could have been present throughout the night.

Another contributing factor to the cloud emission shown in the model in the early part of the mission is the presence of water-ice fog the Phoenix site (Moores et al., 2011). The fog was observed at altitudes as low as 50 m from the surface (Moores et al., 2011), up to 500 m from the surface (Whiteway et al., 2009). On sol 38, the lidar ran its first overnight observation, where ice-fog was detected (Dickinson et al., 2010). The ice-fogs were not observed every sol but increased in frequency as the mission progressed. Similar to the argument above, it is possible surface-level clouds may have formed before sol 38 when the water-vapour abundance was rising, and nighttime temperatures had not yet reached their peak. Possible discrepancies between cloud emission shown in the model, but clouds not detected by the lidar, could be due to the inability for the lidar to see below 200 m (Moores et al., 2011), where ice-fog may have formed. Terrestrial studies show that surface fog can have a marked effect on the downwelling longwave flux, with clouds and fog contributing an additional 77 W m^{-2} to the surface energy balance in Northern China (Guo et al., 2021).

Images taken from Mars Express and Mars Reconnaissance Orbiter throughout the northern summer show an annular cloud that develops each year around $L_s = 120°$ at 60°N (Sánchez-Lavega et al., 2018). Specifically, Sánchez-lavega et al. (2018) note the development of cloud phenomena as a result of a double cyclone that occurred at $L_s = 118°$ during the same time the Phoenix mission was active. The annular cloud is shown to generate nighttime convective instability within the cloud, known as a nocturnal mixed layer (Hinson et al., 2021). Such convection within the cloud leads to increased cloud emissivity and infrared emission (Hinson et al., 2021; Spiga et al., 2017). The increase in cloud emission seen around sol 90 in Figure 2.2a is likely indicative of the convectively active annular cloud reaching the Phoenix site.

On Mars, weather patterns are often discussed in terms of seasonal or diurnal variability. For example, equatorial clouds reach a peak in the ACB season and decline in the dusty season (Madeleine et al., 2012); clouds at the Phoenix site peak overnight and weaken into the morning (Dickinson et al., 2010; Whiteway et al., 2009). This analysis suggests that, in addition to diurnal and seasonal variation, a noticeable degree of sol-to-sol variability exists as well. This variability was noted in the optical depth measurements made by Moores et al. (2010), particularly toward the end of the mission. It was noted that several sols did not show clouds, consistent with this analysis around sol 140. Meteorological modelling from the Phoenix site indicates cloud formation is sensitive to initial moisture availability, so sol-to-sol variability may depend on the advection of air masses past the site (Savijärvi and Määttänen, 2010). Years in which the temporal coverage of the annular cloud were high show a rapid sol-to-sol evolution of the cloud, consistent with this analysis (Sánchez-Lavega et al., 2018).

2.4.2 Model Limitations and Error Analysis

This work uses an energy balance equation and subsurface conduction model to build a record of clouds at the Phoenix site. While care is taken to ensure values in the model are as representative of the Phoenix site as possible, uncertainties do exist and are addressed in this section.

In this work, the air temperature is found by modelling the surface temperature, linking the temperatures through the equation for sensible heat flux. As such, having an accurate ground temperature is important for the modelled air temperature, and ultimately, the cloud emission. Some assumptions were made for the ground temperature parameters, such as keeping the thermal inertia constant over the entire sol. While the thermal inertia changed slightly on diurnal timescales, we use the average value observed to reflect the typical conditions of the landing site.

An error analysis was completed to assess the amount of error in the modelled temperature. Sources of uncertainty include the value for the density of air, ρ_a, which is found using the ideal gas law. As such, the value for ρ_a changes throughout a sol as the temperature and pressure change. For the temperatures and pressures considered, the value for ρ_a has a 7.5% error associated with it. Other variables have errors given in the papers from which they were referenced, such as the surface roughness, z_a, which has an uncertainty of ± 3 mm (Holstein-Rathlou et al., 2010). An error propagation method was then used on the terms in Equation 5, showing the error in the temperature was < 1 K across all temperatures considered.

As mentioned in Figure 2.4, the MET instrument has an uncertainty of ± 1 K. Based on the parameters used in the modelling, it takes 5 W m^{-2} to raise the temperature by 1 K, meaning that the cloud emission values have an uncertainty of ± 5 W m^{-2}. There are several sols, particularly in the beginning of the mission, that have cloud emission values near 5 W m^{-2}. This means that the positive detection of clouds on sols with low R-values may be due to uncertainty in the instrument, rather than the emission of flux toward the surface by clouds

Chapter 3

Updated Visible Opacities of Phoenix Water-Ice Clouds using a Radiative Transfer Model

3.1 Methods

3.1.1 SSI Image Sequences

This work to constrain the optical depths of Phoenix water-ice clouds uses images captured by the SSI on the Phoenix lander. This section will better explain the SSI, as well as the sequential images taken – namely, the ZMs and SHMs.

The SSI was mounted to the mast of the Phoenix lander, locating the camera approximately 1.84 m from the surface. Human stereo vision was simulated by the two eyes of the camera, set 15 cm apart. Twenty-four filters were available for the camera in a range of wavelengths from 447 to 1002 nm, shown in Table 3.1, with each eye having twelve filters. The Charged Coupled Devices (CCDs) for the SSI were flight spare components from the Mars Exploration

Rover (MER) mission, giving pixel arrays of size 1024 x 1024. The field-of-view (FOV) of the full-frame is approximately 14° x 14° (Lemmon et al., 2008).

Table 3.1: Filter Specifications for the SSI, retrieved from (Lemmon et al., 2008).

Filter name	Center Band (nm)	Bandwidth (nm)
L1	673	19
L2	447	23
L3	450.8	4.1
L4	990.7	4.9
L5	887.0	5.8
L6	883	28
L7	802	22
L8	864	37
L9	900	45
LA	931	25
LB	1002	26
LC	968	30
R1	673	19
R2	447	23
R3	671.1	3.9
R4	935.5	5.2
R5	935.7	5.2
R6	450	29
R7	753	20
R8	754	21
R9	753	17
RA	604	15
RB	532	28
RC	485	21

The ZMs were nominally 10-frame sequential 256 x 256 pixel images, with an elevation pointing of 83.79° from the horizon. A difference in elevation angle was chosen for the SHMs to achieve a long path length through the atmosphere – this typically meant the SSI was pointed just above the horizon, or with an elevation angle near 10°. Similarly, the SHMs were composed of 10 frames taken in sequence. These movies were used in previous studies to measure the wind directions, optical depths, and morphologies of clouds above the landing site (Moores et al., 2010).

ZMs were taken as early as sol 6 of the mission, however this work begins using the ZMs collected on sol 48, when both camera eyes were used simultaneously. This means the images taken of the atmosphere can be compared in two wavelengths. Due to the nature of the filter wheel, simultaneous images were taken using the filter pair in the corresponding wheel position. For ZMs, this was commonly the LC/RC or LB/RB pair. SHMs were taken in the same filter pairs, with the first left-eye/right-eye simultaneous SHM collected on sol 58.

The radiometrically corrected (RAD) data files were used for both the ZMs and SHMs. RAD RDRs were generated from EDRs where the usual dark current removal, bias removal, flat-field correction, and bad pixel repair were applied. Pre-flight radiance calibrations were used to scale the images into absolute radiance units of W m^{-2} nm^{-1} sr^{-1}. These units represent the total energy per unit time per unit area per unit solid angle per wavelength received by the camera.

3.1.2 Doubling-and-Adding Radiative Transfer Model

The radiative transfer model used in this work was originally used to study the hazes on Titan (Tomasko et al., 1980), and was adjusted for use in the atmosphere of Mars (Tomasko et al., 1999; Smith and Moores, 2020). The model assumes a plane-parallel atmosphere with a doubling-and-adding (D&A) algorithm for planetary atmospheres (Hansen, 1971). In essence, the D&A method works by solving the radiative transfer equations in an optically thin layer, such that all interactions are described by single scattering. The thickness of the layer is doubled by adding a second layer of the same thickness, and the interactions between the layers are used to calculate the transmission and reflection of energy. This is continued until an atmosphere of a desired thickness is reached.

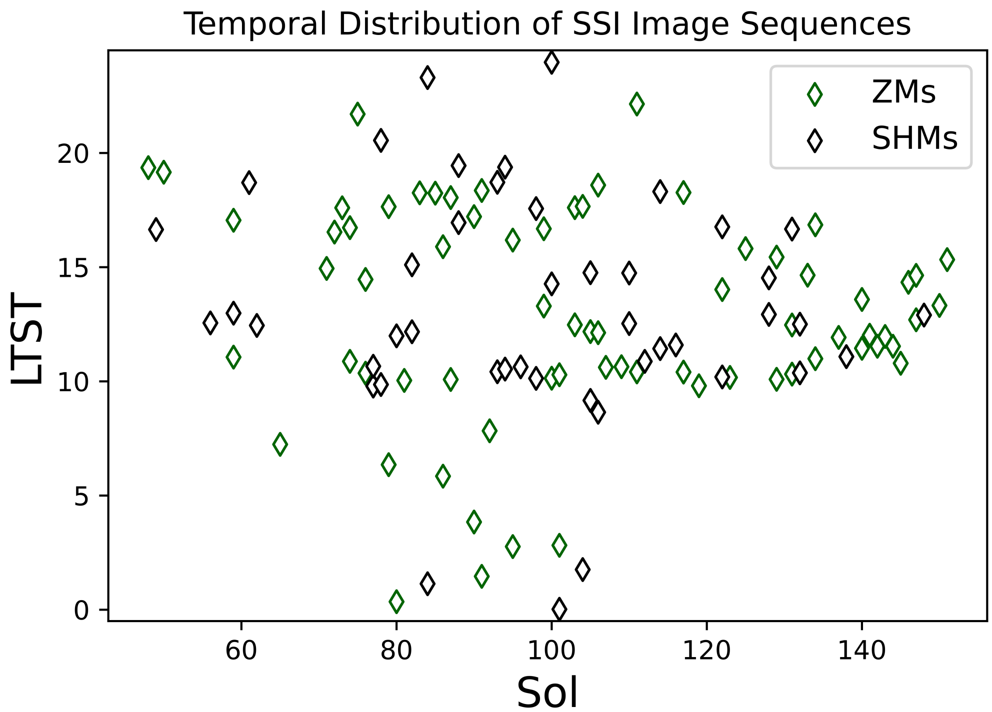

Figure 3.1: Temporal distribution of the SSI images used in this analysis.

In this work, the atmosphere is split into 3 levels with 2 layers. The lower layer of the atmosphere includes Rayleigh scattering due to CO_2 and Mie-scattering dust, while the upper layer contains Mie-scattering due to water-ice particles. Upwards and downwards fluxes and intensities (in W m^{-2} sr^{-1}) are computed at all levels, with appropriate optical depths calculated by the input parameters set for CO_2, dust, and water-ice.

Inputs for the levels in this model are wavelength dependent, covering a range of wavelengths in the visible to near-infrared, as determined by the SSI filters. The most common filters used in this work are the LC, RC, LB, RB, and L4 filters, with respective wavelengths of 968, 485, 1002, 532, and 990.7 nm. For each filter, the model variables are tuned to the specific wavelength to represent their effect in the atmosphere.

In the bottom layer, Rayleigh scattering from CO_2 is included using equation 2.21 in (Hansen, 1971), given as:

$$\tau_R = \frac{P}{g\mu}\frac{(6+3\delta)}{(6-7\delta)}\frac{8\pi^3}{3N^2\lambda^4}(n_g^2 - 1) \tag{3.1}$$

where P is the pressure, g is the surface gravity of Mars with a value of 3.71 ms^{-2}, μ is the mean molecular mass of CO_2 (Hansen and Travis, 1974), n_g is the refractive index retrieved from (Allen and Cox, 2000), dependent on wavelength, λ. N is the number of particles per unit volume at standard pressure and volume (Hansen and Travis, 1974). The depolarization factor, δ, represents the ratio of intensities parallel and perpendicular to the plane of scattering, cited as $\delta = 0.09$ for CO_2 (Hansen & Travis, 1974). In general, the Rayleigh scattering due to CO_2 in the wavelengths considered is small.

Next, the wavelength dependent parameters for dust are needed. The single scattering albedo is found from (Wolff et al., 2009; Tomasko et al., 1999; Johnson et al., 2003). Similarly, the values for the real and imaginary refractive indices are found in the same references, shown in Table 3.2. The size distribution of the particles is represented as a gamma distribution with a geometric cross-section weighted mean radius, r_{eff}, set to 1.6 μm and a variance, v_{eff}, of 0.2 as determined by Tomasko et al. (1999) by examining images taken by the Imager on Mars Pathfinder (IMP).

In the upper layer, water-ice is present. Similar parameters are found for water, shown in Table 3.3, including the single scattering albedo, set to 1 for all wavelengths, as well as the real and imaginary indices of refraction (Kokhanovsky, 2004). For water-ice particles, r_{eff} = 1.5 μm with $v_{eff} = 0.1$ as described by (Guzewich and Smith, 2019) for clouds in Mars' polar region.

3.1.3 Analysis to Find Water-Ice Optical Depth

To find the water-ice optical depth, a combination of the SSI images sequences and D&A model, as described above, are used. Firstly, each frame of a image sequence is averaged

Table 3.2: Wavelength-dependent model parameters for dust

Wavelength	Single Scattering Albedo	Real Index of Refraction	Imaginary Index of Refraction
L4/990.7 nm	0.968	1.4981	0.0045
LC/968 nm	0.935	1.4981	0.00434
RC/485 nm	0.825	1.4981	0.00786
LB/1002 nm	0.948	1.4981	0.00349
RB/532 nm	0.870	1.4981	0.00567

Table 3.3: Wavelength-dependent model parameters for water-ice

Wavelength	Single Scattering Albedo	Real Index of Refraction	Imaginary Index of Refraction
LC/968 nm	1	1.31	10^{-7}
RC/485 nm	1	1.31	10^{-9}
LB/1002 nm	1	1.31	5 x 10^{-7}
RB/532 nm	1	1.31	10^{-9}

together to produce a mean radiance for each pixel in the image. This has the benefit of averaging any small movement in the frame, whether that be the movement of dust or water-ice, to create a "mean" optical depth in the atmosphere.

Dust optical depths were found throughout the mission by Tamppari et al. (2010) in the L4 (990.7 nm) filter. The dust optical depth measurements were constrained to the period around 13:00 - 17:00 LTST for comparison with TES data, which is advantageous for this work because it minimizes possible contimation due to water-ice in the measurements.

We use the dust optical depths found by Tamppari et al. (2010) to constrain the amount of dust in the D&A model. In the model, particle abundances can be specified, returning a corresponding optical depth value for such parameters. For each SSI sequence, dust particles are added into the model until the dust optical depth in the 990.7 nm wavelength matches the values in Figure 3.2. When a sequence is taken at a time where no dust optical depth measurement was taken, an interpolated value based on the nearest measurements is used.

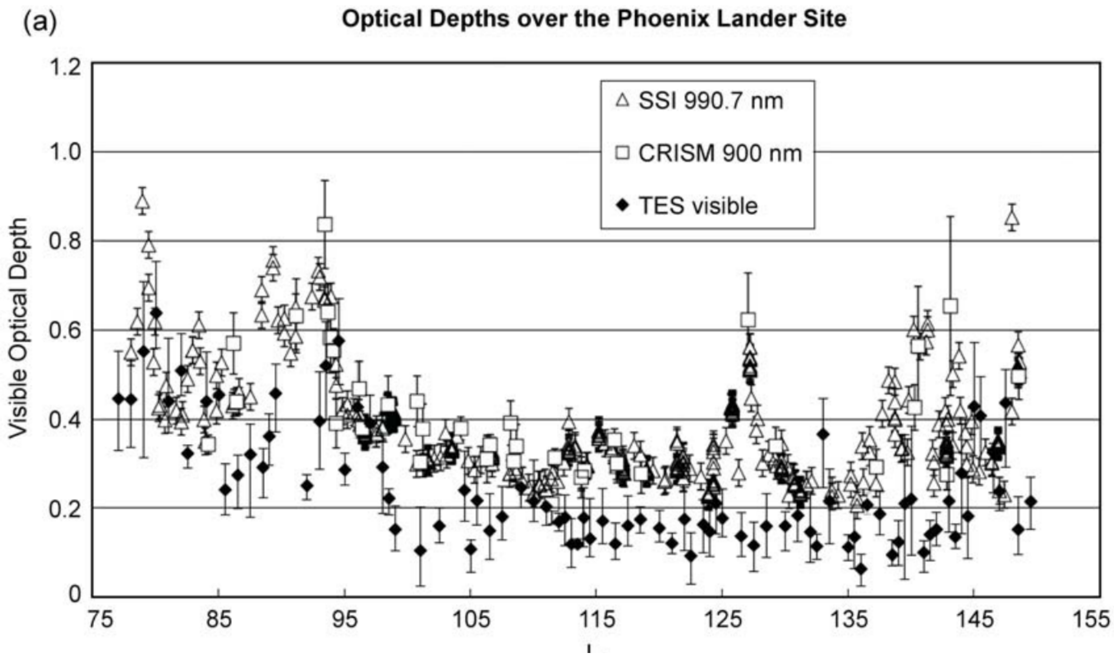

Figure 3.2: From Figure 2a in Tamppari et al. (2010), showing the dust optical depths throughout the Phoenix mission taken in the 990.7 nm filter.

After dust particles are added in to match the D&A model dust optical depth to the value in Figure 3.2, the same dust particle abundance is used as input in the wavelengths for the SSI image being analyzed. At this stage, the water-ice particle abundance is set to 1, giving an water-ice optical depth of 0. The model is run using the Phoenix latitude, local time of the observation, solar longitude, and solar zenith angle as inputs.

The model outputs upwards and downwards intensities at all levels in units of W m^{-2} sr^{-1} within discrete wavelength bands. We are interested in the downwards intensities from the bottom level - i.e. what a camera would see from the surface pointing into the sky. The model splits the sky into 180° azimuth (in 1 - 10° increments), where the sun is always situated at 0° azimuth. In addition, the sky is split vertically from 90° to 0°, representing the zenith angle. The location of the sun in the output is determined by the solar zenith angle given in the input parameters.

For each SSI image, an instrument azimuth and elevation is recorded in the data, specifying the area in the sky at which the SSI is pointing. This information is used to "crop" the model to the SSI FOV, so both the model and SSI are looking at the same point in the sky, with the sun in the same location. Since the sun in the D&A model is always located at 0° azimuth, the azimuthal pointing for the cropped model frame is found by taking the difference between the solar azimuth and SSI azimuth. Lastly, the cropped frame vertical pointing is found by taking 90° - SSI elevation. The SSI image is split into 3 equal horizontal strips, each of which is averaged to get a mean radiance for that section of the image. This is done for easier comparison with the model intensities since the model has gaps in azimuth and elevation angle.

Before comparing the model to the SSI, an additional input parameter to the model must be addressed – the solar flux at Mars in the specific wavelengths being observed. To simplify the procedure, the flux is input to the model as 1 W m^{-2} for all wavelengths used, meaning the model outputs must be scaled to account for the actual flux value. For this, we use the E490 solar spectrum (ASTM, 2000), which takes into account the waveband and solar longitude of the observation, since the amount of solar flux received will vary as Mars moves in its orbit. The model outputs are multiplied by this value of solar flux. Lastly, the outputs are divided by the bandpass for the specific SSI filter, giving radiance in units of W m^{-2} nm^{-1} sr^{-1}, matching the units of the SSI data.

The modeled radiances are compared to the SSI radiances, in both filters used for the respective ZM or SHM. For example, if the LC/RC filters were used for the images, the model is run separately for the 968 nm and 485 nm wavelengths. If the modelled radiances are consistent with the SSI radiances, then the image contains only dust. If the modelled radiances are not consistent with the SSI radiances, cloud particles are added in.

Cloud particles are added into the model in the same manner as dust, which returns an optical depth value based on the specified input parameters for water-ice. After the cloud

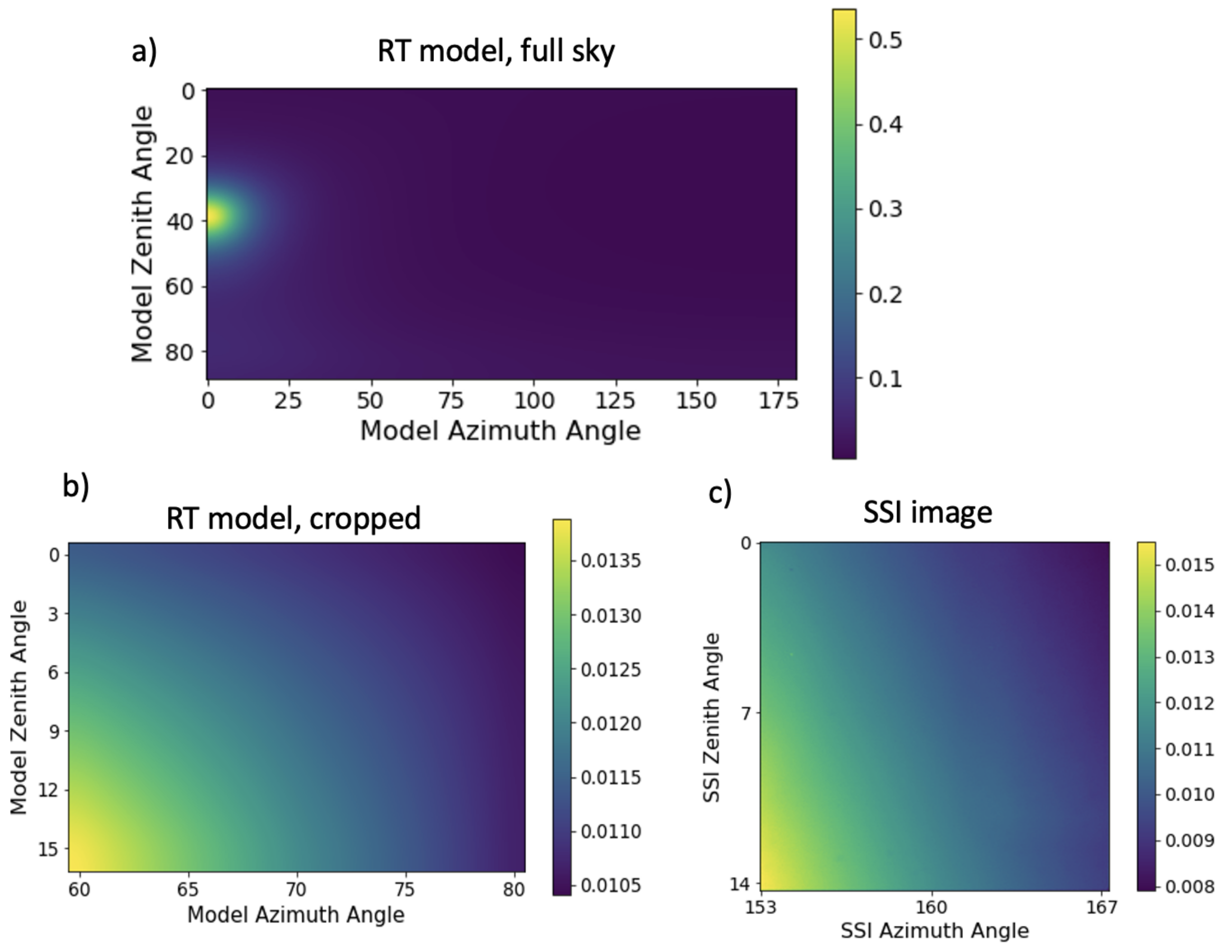

Figure 3.3: The images represent sol 59 at 11:03 LTST. (a) Full sky output from the D&A model. The sun is located at an azimuth angle of 0° and zenith angle of 44°, represented by the high radiance points on the left side of the image. (b) The D&A model output cropped to the FOV of the SSI. (c) The SSI image taken on this sol with an SSI azimuth of 233° and zenith angle of 6°. The D&A model FOV and SSI do not have the exact same dimensions due to the spacing in the model.

particles are added, the radiances from the model and SSI are compared again until the values match. Since the dust and cloud are present in different layers of the model, this gives a total amount of both cloud and dust optical depth, separately. We can analyze all of the ZM and SHMs taken throughout the mission to find any seasonal or diurnal variabilities in the water-ice optical depth.

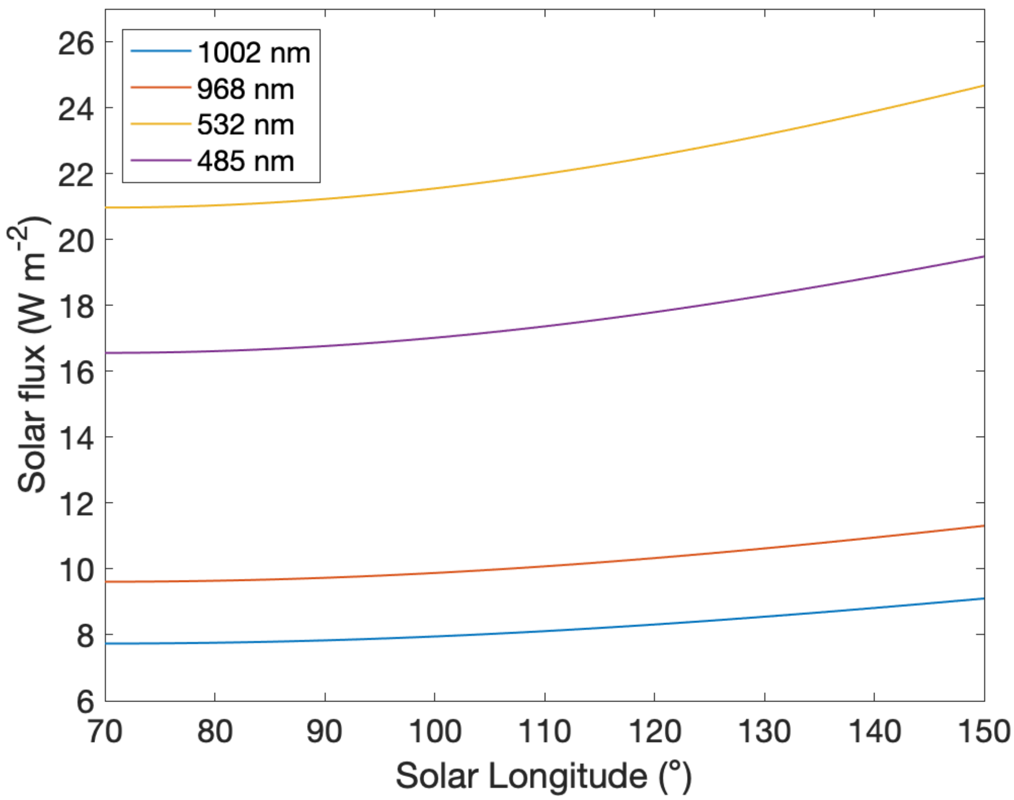

Figure 3.4: The E490 solar spectrum (ASTM, 2000) is used to determine the solar flux at Mars in the wavelengths used by the SSI, namely 1002 nm, 968 nm, 532 nm, and 485 nm. The amount of solar flux at the surface is dependent on both wavelength and solar longitude.

3.2 Results

3.2.1 Zenith Movies

Before beginning to analyze the water-ice optical depths seen throughout the mission using the ZMs, we will look at the comparison between the D&A model and SSI radiances. As mentioned in Section 3.1.3, the water-ice optical depth is found by comparing the modelled radiances to the SSI radiances from an image. As such, when analyzing the images, a slope of 1.0 between the modelled and SSI radiances, once cloud and dust particles are added in, is ideal. This worked well for the LC/RB filters, with the percent error between the predicted and observed values remaining under 10%. However, the RB filter seemed to consistently overestimate the radiance, which can be seen in Figure 3.5b. The points above the red line represent the RB modelled radiances, while those on the line represent the LB radiances. Because of this consistent overestimate, when the LB/RB optical depths are reported below, note that a 30% error between the modelled radiance and SSI radiance in the RB wavelength is used as a baseline.

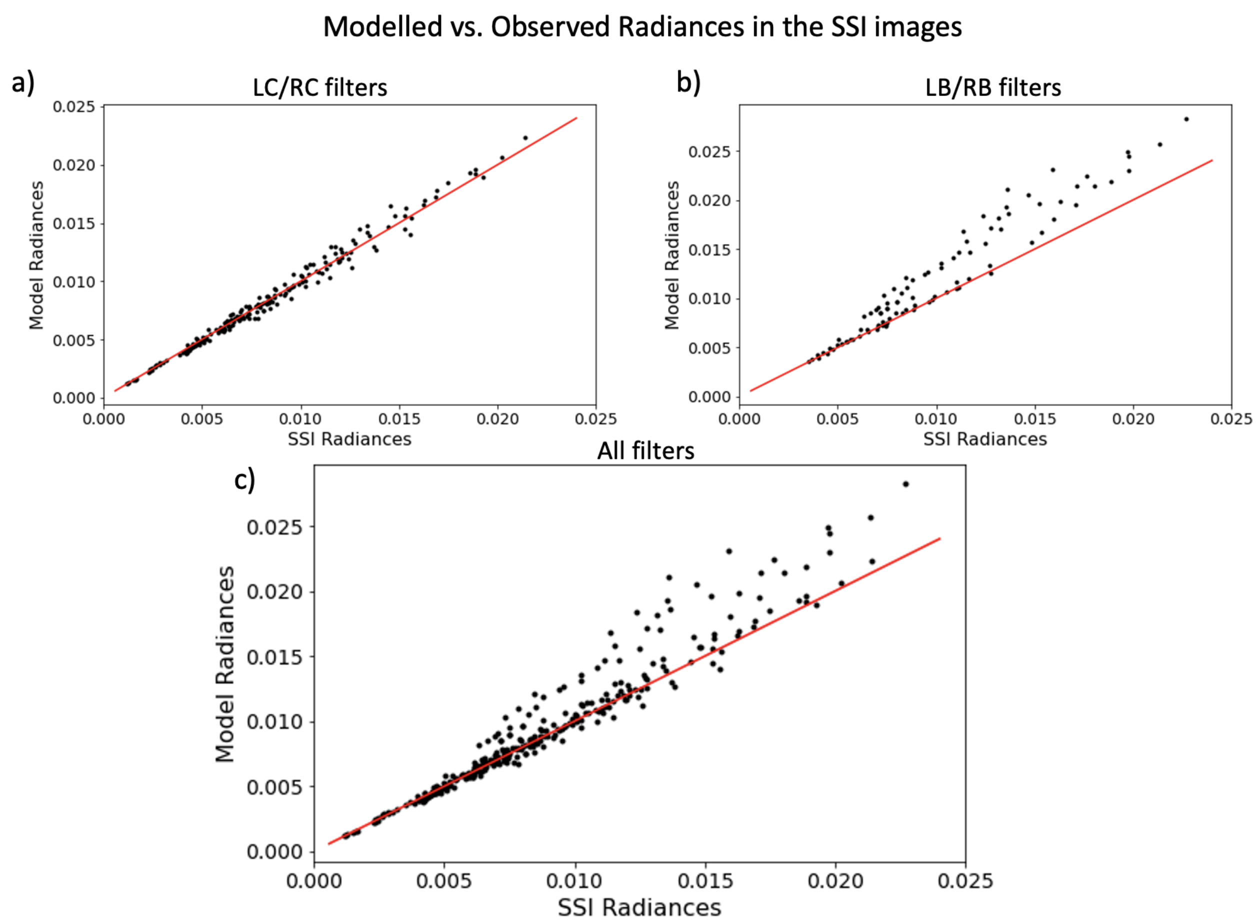

Figure 3.5: Modelled vs. observed radiances in the ZMs, using the (a) LC/RC filters, (b) LB/RB filters, (c) both LC/RC and LB/RB filters together. The red lines represents a 1:1 ratio between the modelled and observed results. The RB filter was largely overestimated by the model, with a baseline 30% error. However, the LC/RC and LB filters did not have this overestimate.

Of the sixty-four ZMs taken throughout mission, a non-zero water-ice opacity was found for thirty-four image sequences. As shown in Figure 3.6, the water-ice opacities range in value from 10^{-3} to 10^{-1}, which is consistent with the thin, often sub-optical, clouds imaged throughout the mission. It is important to note that the particle sizes used in this calculation

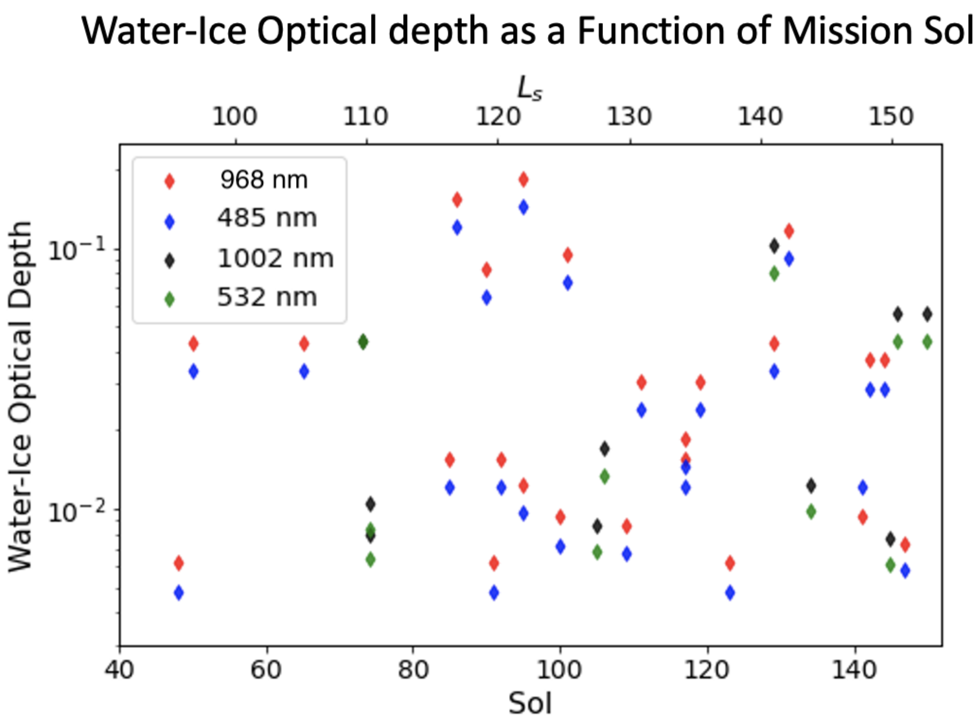

Figure 3.6: Optical depth of water-ice clouds throughout the Phoenix mission derived using SSI-captured ZMs and the D&A model. The optical depths are given in the LC/RC and LB/RB filters. The water-ice optical depths are consistent with the thin clouds observed at the Phoenix landing site.

are small, while larger particles may be more representative of the Phoenix landing site (Whiteway et al., 2009). Larger particles may scatter light differently, potentially using Henyey-Greenstein scattering instead of the assumed Mie scattering. However, the order of magnitude of the water-ice optical depths would not be expected to vary drastically based on previous literature (Dickinson et al., 2010; Moores et al., 2010; Tamppari et al., 2010).

Because ZMs were captured with only one filter prior to sol 48, we are not able to make comparisons of optical depths throughout the entire mission. Instead, we begin on sol 48, and continue through the mission. The peak in optical depths in Figure 3.6 occurs around sol 90, at $L_s = 118°$. Summer solstice at the Phoenix location occurs at $L_s = 90°$, however the maximum solar insolation, and maximum air temperature, peaks around mission sol 60, or $L_s = 105°$, due, in part, to Mars' position in its orbit. By the time of the highest opacities observed in Figure 3.6, the air temperature is on a decline. The optical depth drops for the next ~20 sols, increasing again around sol 130, when $L_s = 140°$.

The same data can be plotted as a function of LTST, rather than mission sol, to investigate any diurnal variability in the opacity. This is shown in Figure 3.7.

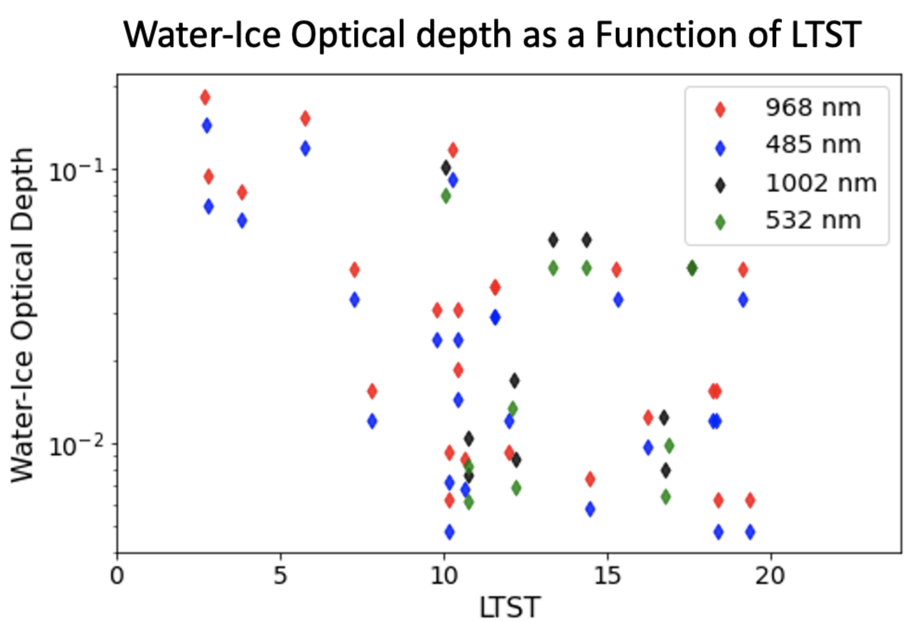

Figure 3.7: Optical depths of water-ice clouds is recorded as a function of LTST. The highest optical depths are recorded throughout the night, while the late morning and afternoon optical depths are lower.

When comparing the filters, the water-ice optical depth tends to be larger in the longer wavelengths. When an image is taken with the LC/RC pair, the water-ice opacity is higher in the 968 nm filter, compared to the 485 nm filter. The same is true of the 1002 nm and 532 nm filters, representing the LB/RB pair. While somewhat difficult to discern due to the logarithmic scale in Figure 3.6, as the opacity increases, the differences between the two opacities increases, as well. For example, on sol 95, the difference between the opaicities in the LC and RC filters are 0.0124 and 0.00997, respectively. However, another image analyzed on sol 95 shows higher optical depths, with the LC filter giving an optical depth of 0.1854 and the RC filter having an optical depth of 0.1449.

Since the clouds change both seasonally and diurnally, the most complete picture of the water-ice optical depth comes from combining both mission sol and LTST. This is shown in Figure 3.8. The data points with the highest optical depths, although occurring earlier in the mission when the overnight temperature is warmer, occur at the coldest time of a sol,

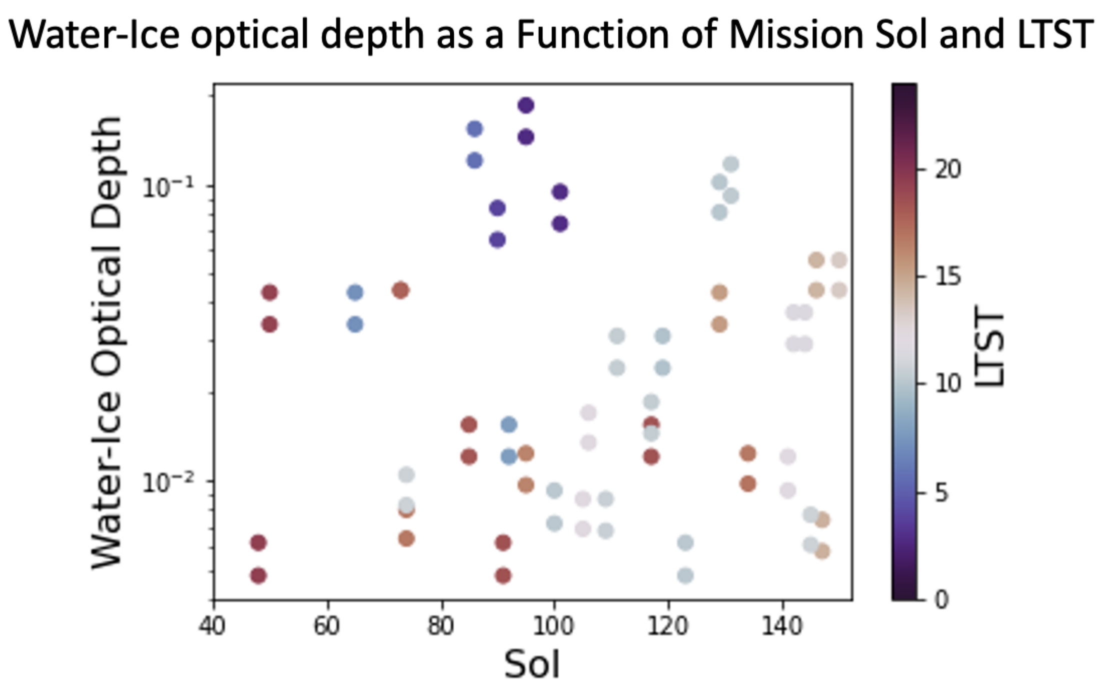

Figure 3.8: Water-ice optical depth of the SSI sequences as a function of both mission sol and LTST. This highlights both the seasonal and diurnal trends throughout the mission. The water-ice opacity increases both into the night, and as the mission progresses past summer solstice.

between 2:00 and 5:00 LTST. When the data from similar times are analyzed – from ∼10:00 to ∼18:00 LTST – a clear increase in opacity toward the end of the mission can be seen, suggesting clouds towards the end of the mission were optically thicker than clouds observed in the middle of the mission.

Many of the image sequences analyzed throughout the mission had a non-zero value for water-ice optical depth, however, there were several sols analyzed that had an optical depth of zero, shown in Figure 3.9. There were 15 sequences with a water-ice opacity of zero, spread quite evenly between sol 70 and sol 150, with perhaps the largest gap occurring between sols 90 and 120. All of the sequences were captured between the hours of 10:00 and 20:00 LTST. Since there were fewer nighttime sequences captured, it is difficult to say if this is due to clouds consistently forming each night with a non zero optical depth, or a lack of data. Additionally, since ZMs were not captured until sol 48, it is possible the beginning of the mission would have an increase in images without any cloud.

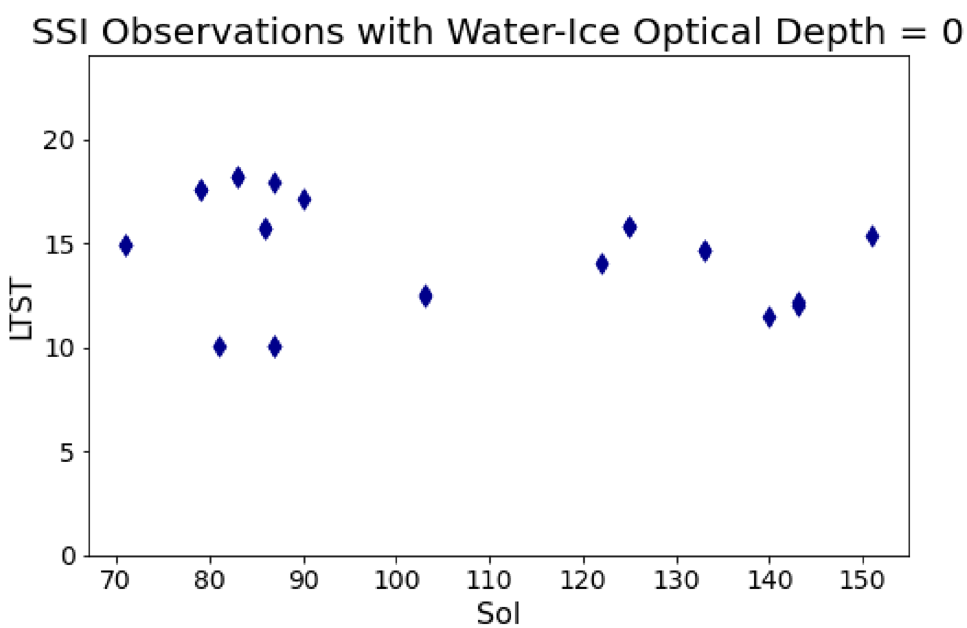

Figure 3.9: ZM image sequences showing no cloud throughout the mission. Most of the sequences containing no clouds were captured between the hours of 10:00 and 20:00 LTST, spread quite evenly throughout the mission.

3.2.2 Supra-Horizon Movies

Similar to the ZMs, the LB/RB filter pair in the SHMs had an approximate 30% error for the radiances in the RB filter. However, unlike in the ZMs, the RC filter also experienced consistently high modelled radiances compared to the radiances in the SSI images. These radiances are shown in Figure 3.10. Similarly to the ZMs, the baseline of 30% error is accepted for the RB and RC filters, and the LB and LC filters are based off their 1:1 ratio with the SSI radiances.

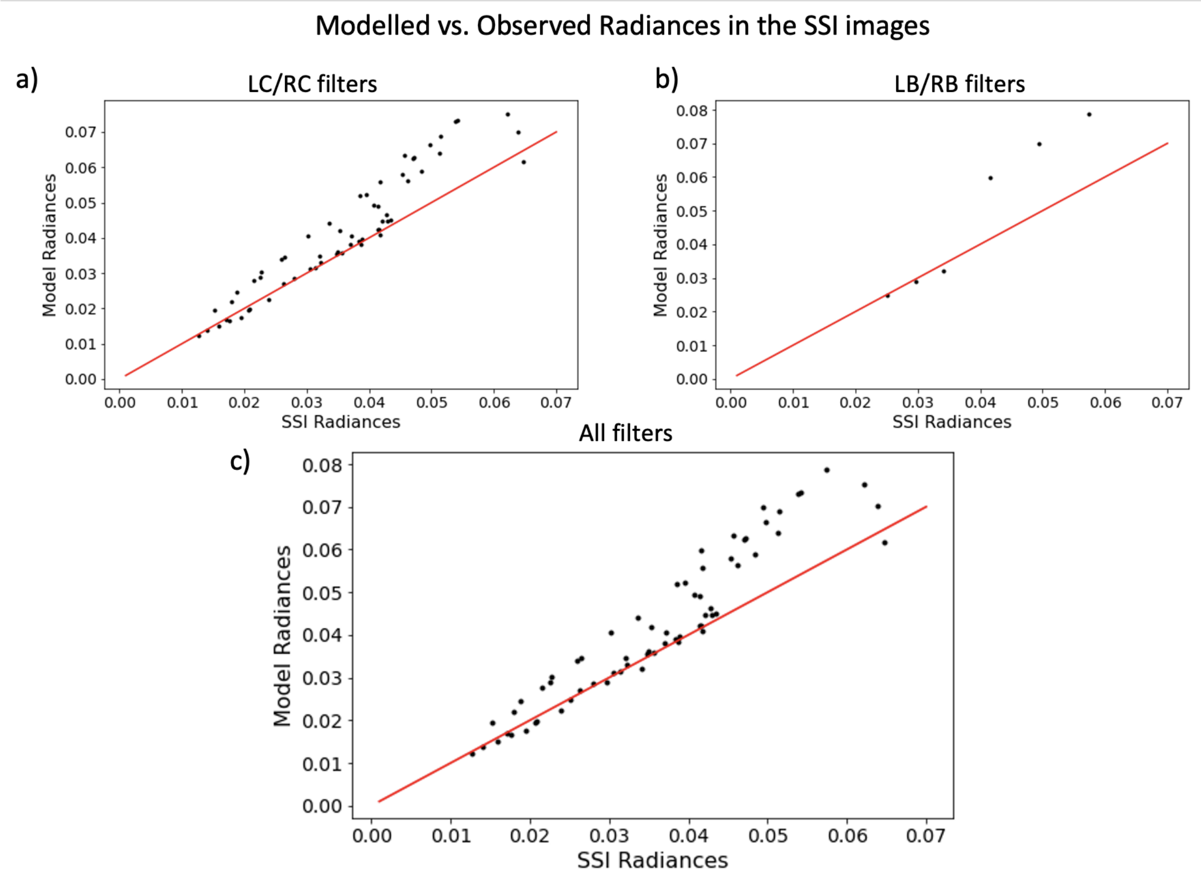

Figure 3.10: Modelled vs. observed radiances for the SHMs used in this analysis. The radiances are observed in the (a) LC/RC filters, (b) LB/RB filters and (c) both the LC/RC and LB/RB pairs. The red line represents a 1:1 ratio between the modelled and observed radiances. The RB and RC filters often modelled much higher than observed in the SSI images, so they were taken with a ~30% error baseline.

Unfortunately, many SHMs were rejected in this analysis, which is explored in section 3.3.1. Of the thirty-eight total SHMs, only six are considered in this analysis with a nonzero water-ice optical depth. Five of the six SHMs were captured using the LC/RC pair and one was taken in the LB/RB pair, as shown in Figure 3.11. The optical depth values are consistent with what would be expected from clouds above the Phoenix site, with values between 10^{-2} and 10^{-1}.

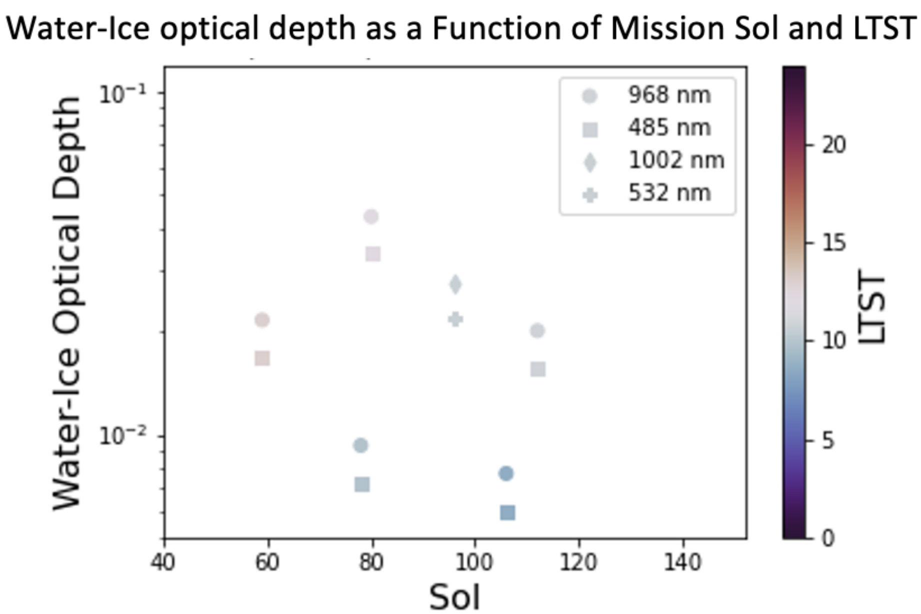

Figure 3.11: The water-ice optical depth is plotted as a function of mission sol and LTST to bring out any seasonal and diurnal trends in the data. While the optical depth values are similar to what would be expected from Martian clouds, the limited data means patterns are not discernible in the data.

Due to the lack of useful results, diurnal and seasonal trends are not easily determined in the SHM opacities. Each data point is within the time frame from 10:00 to 15:00 LTST, on mission sols 60 to 120. Without additional data, it is difficult to determine if nighttime measurements would lead to high optical depths, as noted within the ZM opacities. The same is true for measurements taken later in the mission, after sol 120. Similar to the ZMs, the longer wavelength (ie. the LB/LC filters) has the higher opacity compared to the filter in the pair with the shorter wavelength.

There were five SHMs with a water-ice optical depth of zero, shown in Figure 3.12. Similar to the ZMs, the images with no clouds were taken between 10:00 and 20:00 LTST, spread evenly from sol 75 to sol 110. Because of the number of SHMs that were rejected due to the high radiances, it is likely there are more sols without clouds that are not captured in this data.

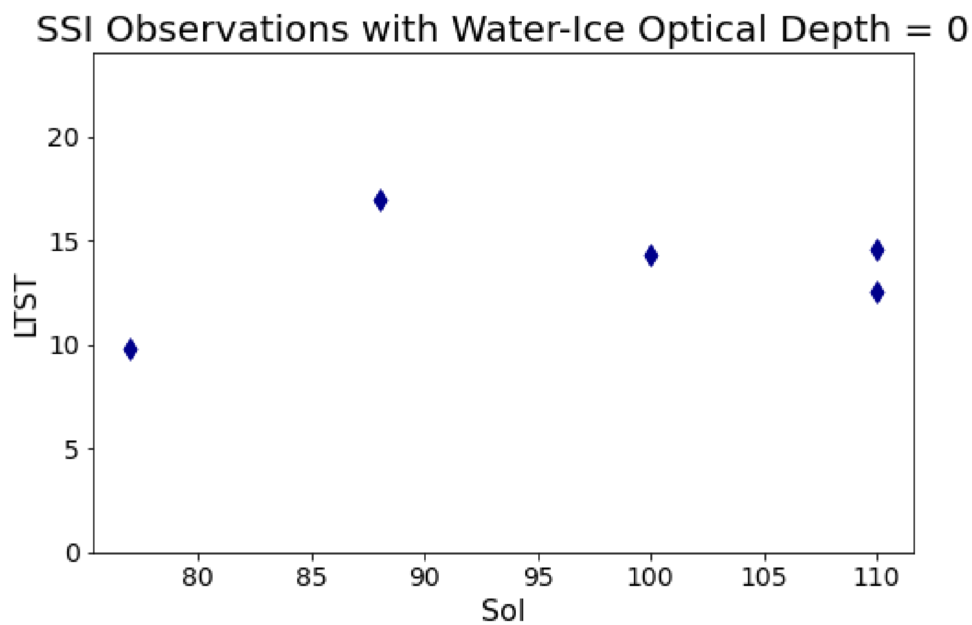

Figure 3.12: SHMs with a water-ice optical depth of zero. The images were all captured between 10:00 and 20:00 LTST, with an even spread from sol 75 until sol 110.

3.2.3 Comparison to Moores et al. (2010)

This work was motivated by the desire to constrain the water-ice optical depths observed by the SSI onboard the Phoenix lander. As such, we compare the opacities found using the D&A model to those derived by Moores et al. (2010) using an MFS method. The optical depths found in the ZMs using both methods are compared in Figure 3.13. It is important to note that Moores et al. (2010) found the optical depth of the variable layer in the images, therefore some of the optical depths may include more dust than water-ice.

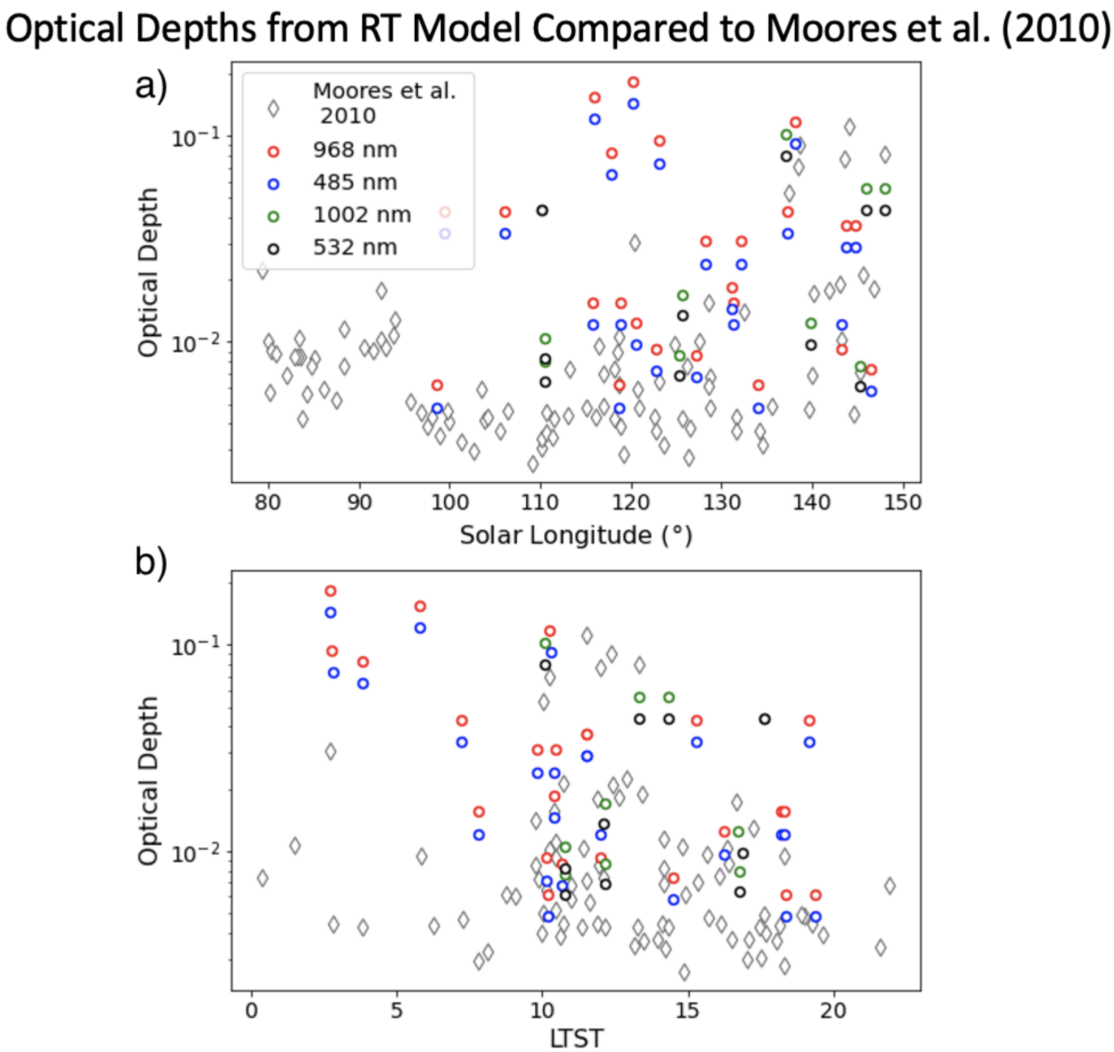

Figure 3.13: Comparison of water-ice optical depths derived with the D&A model to those reported in Figure 6 by Moores et al. (2010). The water-ice opacities are shown as a function of (a) L_s and (b) LTST. In general, the derived optical depths are very similar, particularly the increase in opacity toward the end of the mission. The D&A model gives higher opacities for images taken between 2:00 and 10:00 LTST

It can be seen in Figure 3.13 that the optical depths from Moores et al. (2010) are similar to those derived using the D&A model, particularly in the rising trend toward the end of the mission. In the L_s range from 100° to 130°, the opacities are close in value, with the D&A

model giving slightly higher results. There are a couple points around $L_s = 120°$ where the D&A model gives much higher values – up to 10^{-1}, which is not seen with the MFS method – but this is analyzed in Figure 3.13b. From $L_s = 130°$ until the end of the mission, both this work and Moores et al. (2010) show an increase in opacity, with similar values. Unfortunately, since images were not taken in filter pairs until sol 48, we are unable to compare opacities before $L_s = 100°$.

Comparing the opacities as a function of LTST, several noticeable differences arise. In the late morning to evening hours, around 10:00 to 18:00 LTST, the opacities are quite similar. However, between the hours of 2:00 to 10:00 LTST, the D&A model gives much higher values than shown in Moores et al. (2010). This work does not have any overnight opacities from 20:00 to 2:00 LTST to compare to the data points in Moores et al. (2010).

3.2.4 Comparison to Cloud Emission

In Chapter 2 we explored the radiative influence of clouds above the Phoenix landing site. In Figure 2.4, the water-ice optical depths retrieved from the lidar were compared to the thermal cloud emission derived from modelling the MET temperature data. Here, we use the water-ice optical depths from the ZMs in the 532 nm filter to compare to the cloud emission found in Chapter 2. This is shown in figure 3.14, where six ZMs fell within the 22:00 to 10:00 LTST time-frame explored in Chapter 2. The 532 nm filter is selected for comparison with the lidar optical depths as the laser operated at 532 nm.

This analysis is consistent with that of Chapter 2, where optically thicker clouds tend to radiate more energy toward the surface. The clouds associated with the D&A-derived optical depths emit around 7 to 10 W m^{-2} of radiation toward the surface, with the highest cloud emission of 20 W m^{-2} coming from a water-ice optical depth of 0.1449. Additionally, these points fall within the expected temperatures for water-ice clouds on Mars.

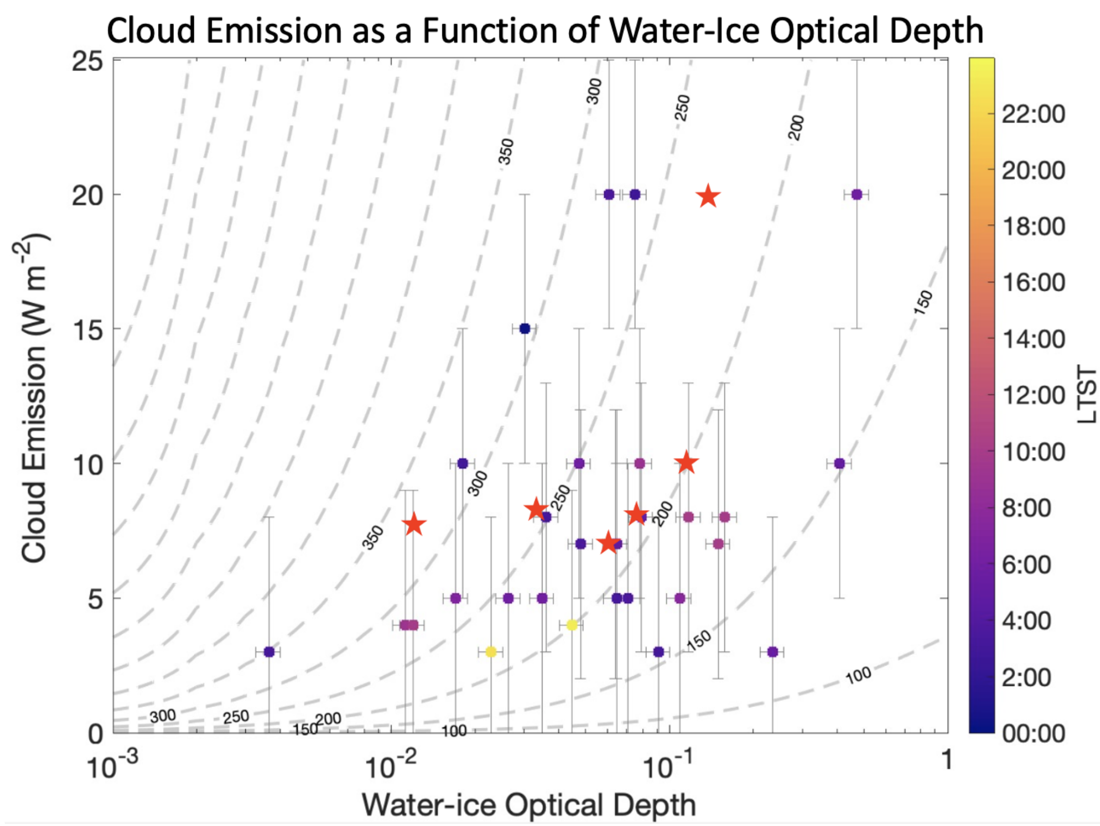

Figure 3.14: Cloud emission is shown as a function of water-ice optical depths derived from the lidar (circles) and D&A model (red stars). The D&A model points all fall within 2:00 to 8:00 LTST. The cloud emission and optical depths from this analysis are consistent with those derived from the lidar.

3.3 Discussion

3.3.1 Discussion of Uncertainties

For both the ZMs and SHMs, several image sequences were rejected in this analysis. Fifteen ZM sequences were rejected and twenty-eight SHMs were not included. Particularly for the SHMs, since many more sequences were rejected than accepted, an investigation into this discrepancy will be discussed here.

As mentioned in section 3.2.1, A 30% error was used as the baseline between the D&A model and the SSI images in the RB filter, but the LB filter was largely consistent between the observed and predicted radiances. This was not always the, case, however, and the LB filter sometimes also modelled unrealistically high. The same is true for the LC/RC filter. Due the way the analysis is carried out, if the D&A model is predicting radiances that are too high when only dust particles are present, water-ice particles are not added as they would only further increase the radiance. In such a case, the image cannot be accepted because the water-ice content of the atmosphere is inconclusive. Therefore, images were rejected on two bases: 1) both of the filters in a pair are modelling too high and 2) both of the filters in a pair are modelling unrealistically low, such that only a nonphysical amount of cloud particles are needed to match the radiances between the D&A model and the SSI images. The second scenario occurred much less often than the first.

Figure 3.15 shows the relationship between the observed and predicted radiances for the rejected ZMs and SHMs. As noted, most of the modelled radiances are much higher than observed, which only worsens as the radiances increases.

We explore several variables in the images to determine if there may be a common factor that is resulting in the radiances modelling too high. First, we examine the temporal distribution of the rejected images. At first glance, there does not appear to be a strong correlation between the rejected sequences and the time-of-day. However, it is important to note that all of the sequences where the D&A model was giving radiances that were too low occur between the hours of 22:00 and 2:00 LTST. This suggests there is an issue where the D&A model underestimates the radiances when the solar zenith angle is too high - or in other words, when the sun is too low in the sky.

The rejected images outside of the midnight to 2:00 time-frame are spread evenly between 10:00 and 20:00 LTST. These are the images where the modelled radiances were too high. Because of the even spread of the data over sol and time, it cannot be certain that any one solar zenith angle, or range of solar zenith angles, is causing the model to overestimate the radiances. Particularly when compared to Figure 3.1, many images within this time-frame

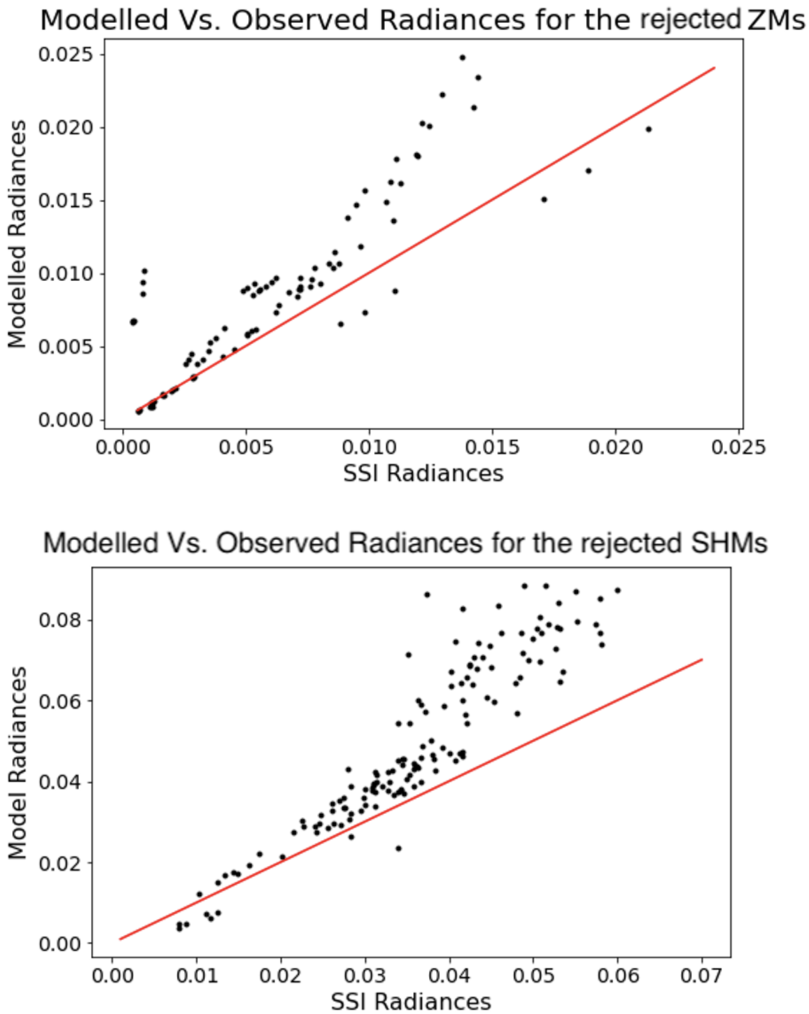

Figure 3.15: Modelled vs. observed radiances for the rejected image sequences. The modelled values often have much higher radiances than the values captured in the SSI images, which becomes even larger with an increase in radiance. Fifteen ZMs were rejected, while twenty-eight SHMs were rejected because of this discrepancy.

were accepted, meaning the model can accurately predict between the hours of 10:00 and 20:00. This suggests there may be another problem causing the discrepancy when the modelled values are too high.

Next, we examine whether the azimuth angle used in the D&A model has any effect on the radiances, which is shown in Figure 3.17a. The azimuth angle used in the D&A model is not the "true" azimuth angle (based on the convention chosen by the Phoenix team), but the

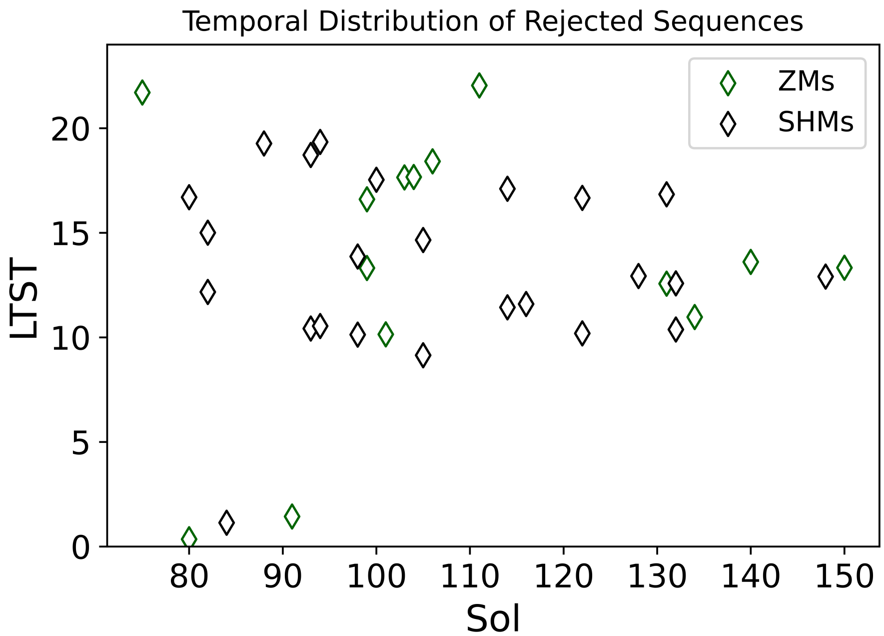

Figure 3.16: Temporal distribution of the rejected SSI image sequences. The sequences between the hours of 22:00 to 2:00 were rejected due to unrealistically low radiances, while the others were rejected due to unrealistically high radiances.

difference between the solar azimuth angle and the SSI azimuth angle. Both the accepted and rejected sequences are used in this figure to illustrate comparison. As seen in Figure 3.17a, the majority of the rejected SHMs have an azimuth angle of 45°, while a couple have a solar azimuth angle around 90°. However, several of the accepted SHMs are also near the 45° mark. Both the accepted and rejected ZMs have a larger spread in solar azimuth angle.

No certain claim can be drawn from observing the spread of azimuth angles, particularly when it comes to the rejected ZMs, as they seem to be spread randomly. The large concentration of rejected SHMs at 45° could suggest the model struggles to recreate the radiances at this angle, but it may likely be the case that another issue is causing the high radiances, and that a majority of SHMs were coincidentally taken with this azimuth angle, implying a correlation that does not actually exist.

Next, we observe whether the dust opacity is causing the high radiances in the D&A

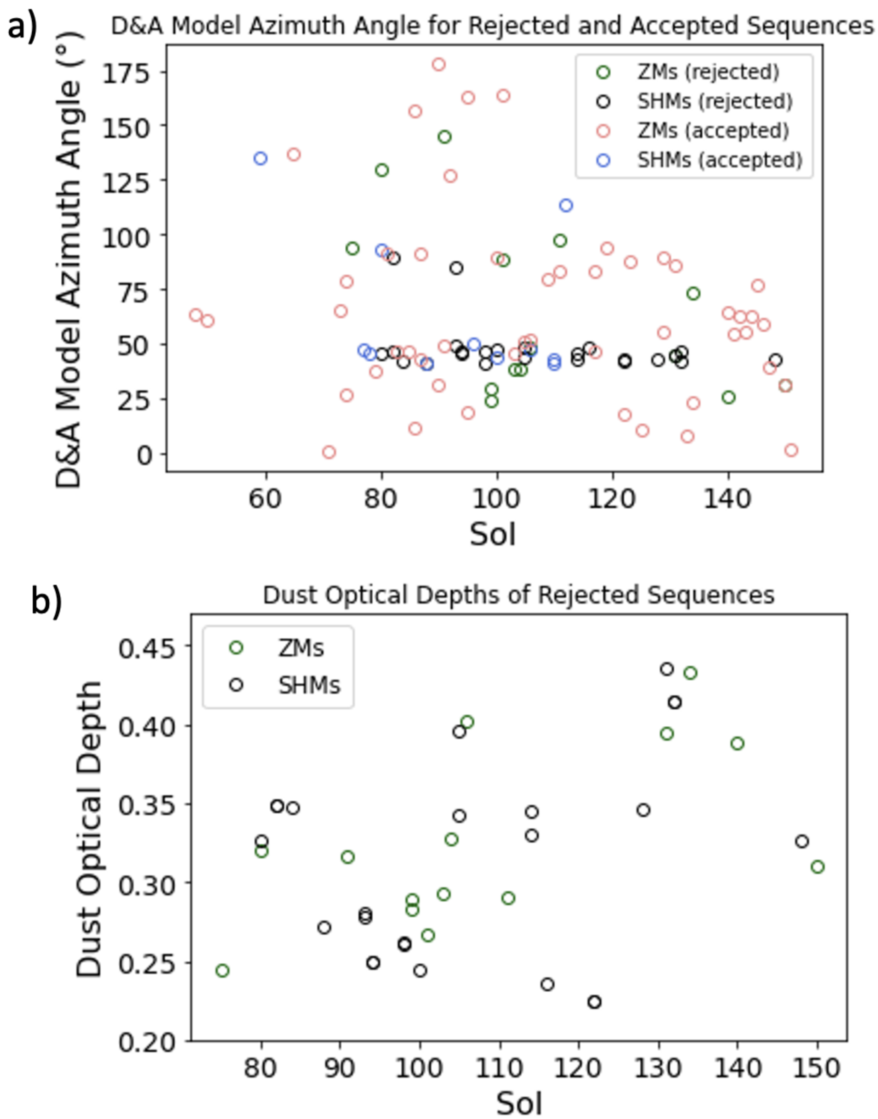

Figure 3.17: (a) The azimuth angle used in the D&A model as a function of mission sol for both accepted and rejected images. While most rejected SHMs occurred at an azimuth angle of 45°, many of the accepted images also occurred at this angle. (b) Dust opacity as a function of mission sol for the rejected sequences. There does not appear to be any pattern in the dust opacity resulting in radiances that are too high.

model. The dust optical depth of each rejected sequence is shown in Figure 3.17b. The dust opacity is a particularly important variable because the amount of dust loading in an image has a strong effect on the radiance. In Figure 3.17b, there is no pattern between the rejected images and the dust optical depth, with a range of values between 0.20 and 0.45.

Even without a correlation in Figure 3.17b, the dust opacity may play an important role in the uncertainty. As mentioned in Section 3.1.3, the dust opacities from Tamppari et al. (2010) were used to constrain the amount of dust in each image. The dust observations were taken between 13:00 - 17:00 LTST, meaning the dust opacity may have varied in images taken outside of these times. While the dust in Figure 3.2 remains largely consistent from sol-to-sol, there has also been observations of dust opacity varying on shorter timescales within each sol (Tamppari et al., 2010). If this is the case, it is possible that an overabundance of dust has been added to some of the model runs, increasing the radiances in the D&A model compared to what would is observed in the image.

It is unclear what factor is responsible for producing the high radiances in the D&A model. In fact, it could be a combination of several factors. Another point to remark is that the SHMs usually had an SSI elevation angle of $\sim$10°, compared to the ZM SSI elevation angle of $\sim$83°. It is possible that the low elevation angle of SHMs, which ensures a longer path length through the atmosphere, in combination with an inaccurate dust abundance, may be leading to the model overestimating the radiances in the SHMs more often than the ZMs. Methods to improve the uncertainties will be discussed in Chapter 5.

3.3.2 Comparison to Prior Studies

Figure 3.13 compares the water-ice opacities derived from Moores et al. (2010) with those derived using the D&A radiative transfer method. As mentioned, the results are largely similar, with the greatest deviation occurring in the hours before 10:00 LTST, where this work shows higher opacities than Moores et al. (2010). Previous studies, including Chapter 2, have shown that the clouds tend to be thickest throughout the night when the temperatures are coldest (Dickinson et al., 2010). This method of finding the water-ice optical depth validates that conclusion, suggesting the D&A method better constrains the water-ice optical depths, particularly during the time-frame between 2:00 to 10:00 LTST. However, while image sequences were rejected when the solar elevation angle was too low using the D&A model, the MFS method is able to find a lower limit in the opacity.

The visible opacities derived in this work are consistent with the thermal emission modelled in Chapter 2. The clouds emit thermal radiation at temperatures that are expected due to the temperature of the Martian atmosphere. Making a direct comparison between visible opacity and thermal emission, as shown in Figure 3.14, allows us to directly assess the effect of the clouds on the surface energy balance, and therefore, the weather and climate at the Phoenix landing site.

Chapter 4

Conclusions

This work analyzed the water-ice clouds above the Phoenix mission landing site by analyzing their interaction with shortwave and longwave radiation. Firstly, in Chapter 2, by modelling and comparing the 2 m atmospheric temperature to the data collected by the MET temperature sensor, the amount of radiative flux emitted by clouds toward the surface is modelled. This allows us to put together a full record of clouds throughout the Phoenix mission, filling in temporal gaps in the cloud record left by the SSI and lidar.

Longwave flux emitted from clouds is shown to increase through the night, typically starting no earlier than 22:00 LTST and ending no later than 10:00 LTST. For the first 50 sols, the cloud emission is consistently under 10 W m^{-2} for a given night, with a few sols showing no flux. Between sols 50 and 80, the frequency of nights with no cloud emission reached a maximum. When clouds formed during this time, R is shown to become positive only later in the night, when the air temperature is the coolest. From sol 90 onward, the maximum cloud emission values are modeled, periodically reaching 20 W m^{-2} or more.

The additional flux supplied to the surface by the nocturnal clouds induces a thermal effect, slightly warming the ground and overlying air. For most sols, the warming is between 1 and 3 K, with the highest warming of 8 K occurring at the end of the mission. Integrating the flux over each sol shows that the energy balance follows a typical seasonal pattern, as the energy balance is dominated by the solar and outgoing longwave flux terms. However, R is much more variable than other components of the energy balance, suggesting that cloud formation is dictated by small-scale effects.

We explicitly link the optical depth of the clouds with their radiative contribution to the surface energy balance. Comparing the cloud emission with water-ice optical depth values from Dickinson et al. (2010), we show that a cloud with a higher optical depth radiates more energy to the surface. By examining the time of day when the optical depth and R are highest, it can be seen that clouds give off the most energy to the surface in the early morning hours, around 4:00–6:00 LTST. Additionally, the cloud emission was further validated by the retrieval of cloud temperature as a function of emission and water-ice optical depth. Within error, each cloud temperature was within the expected temperature for the Martian atmosphere.

In the visible wavelengths analyzed in Chapter 3, we used a D&A radiative transfer model to constrain the water-ice content in SSI image sequences. This was achieved by adding in dust and water-ice particles so that the modelled radiances matched radiances in the SSI images. This allowed us to analyze the variability in water-ice optical depth, as well as compare this method to prior methods.

The water-ice optical depths were observed in several wavelengths – 968 nm, 485 nm, 1002 nm, and 532 nm. The opacity, especially as observed in the ZMs, increased throughout the mission, and the highest opacities occurred between the hours of 2:00 to 5:00 LTST. This is consistent with the cloud emission results derived in Chapter 2.

Comparing the results derived using the D&A model in this work and the MFS procedure used by Moores et al. (2010), the water-ice optical depths during the daytime are shown to be consistent. The same increase toward the end of the mission is observed in both studies. Differently, however, are the opacities between the hours of 2:00 to 10:00, where this work gives higher optical depths, while the MFS method gives lower optical depths. Unfortunately, because the D&A model underestimates the radiances at low solar elevations, the opacities between the hours of 22:00 to 2:00 cannot be compared.

Lastly, we analyzed several sources that may be causing the D&A model to return radiances that are much higher than seen in the SSI images. The time of observation, azimuth angle, and dust opacity were all explored, however one single variable could not be determined to be the sole cause of the discrepancy. Because many more SHMs were rejected than accepted, it is possible the model is struggling to recreate the radiances at the long path lengths observed in the images. Future work will seek to correct the high radiances, resulting in more opacity data throughout the Phoenix mission.

Chapter 5

Future Work

There are several ways to expand the investigation into the interaction between water-ice clouds and radiation. Firstly, it is crucial to extend this work globally. Both Chapters 2 and 3 focus on the water-ice clouds at the Phoenix landing site. As the most northern-based lander, the Phoenix site offers a unique perspective on clouds in the polar region of Mars, however, water-ice clouds form at many locations around the planet. Understanding the microphysics of the clouds and their resulting effect on the weather, climate, and dynamics of the atmosphere requires a larger, global picture.

One way to extend this work is to apply the techniques used at other landing sites that have spacecraft with meteorological stations. Currently, an analysis into effects of longwave radiation from water-ice clouds has been carried out at the MSL landing site in Gale Crater (Cooper et al., 2021) and the Phoenix landing site, shown in Chapter 2. However, other surface spacecraft, such as InSight and Mars 2020 (Perseverance Rover), also carry their own meteorological stations, measuring, at minimum, the near-surface air temperature (Spiga et al., 2018; Rodriguez-Manfredi et al., 2021). The record of air temperature recorded from these missions can be used as in Chapter 2 to build a record of clouds.

The Mars Environmental Dynamics Analyzer (MEDA) on Mars 2020 may prove especially useful for expanding this work. MEDA contains several temperature sensors to monitor the temperature at 0, 0.84, 1.45, and 40 m from the surface, with data acquired at a rate of 2 Hz when commanded (Rodriguez-Manfredi et al., 2021). In addition, MEDA has a Thermal Infrared Sensor (TIRS) to measure the downwelling and upwelling longwave radiation, reflected shortwave radiation from the surface, among other properties. These quantities are very useful for analyzing the radiative contribution of water-ice clouds. In Chapter 2, the terms in the energy balance had to be modelled, introducing inherent uncertainty into the calculation. Analyzing the downwelling longwave radiation received by TIRS with and without clouds can give insight into the amount of radiation emitted toward the surface empirically. In addition, combining the TIRS data with atmospheric images to calculate water-ice optical depth, a direct comparison of water-ice optical depth and cloud emission can be found. Lastly, this can be linked to the temperature data retrieved by the temperature sensor to further constrain the impact of the water-ice clouds above the rover.

As mentioned in Section 3.3.1, further work is needed to constrain the water-ice optical depths at Phoenix landing site. Only six SHMs were included in this work, meaning a great deal of information about the water-ice clouds is missed due to problems in the analysis. Firstly, the excessively high radiances need be addressed in future work. As mentioned, one of the potential contributing problems to the high radiances may be due to the uncertainty associated with the dust opacity, where image sequences taken outside of the 13:00 to 17:00 LTST range do not have an associated dust opacity and must be inferred. We can use the bispectral nature of the SSI image sequences to address this concern.

Most of the SSI sequences were taken in the LC/RC and LB/RB image pairs, where LB/LC are longer – and, therefore, redder – wavelengths than the RB/RC filters. Martian dust appears brighter in red wavelengths compared to blue wavelengths, whereas water-ice particles will have similar brightness in both red and blue. Using the LB/LC wavelengths, dust particles can be added into the D&A model until the radiances match those in the redder filter. This can be used as a calibration step. Then, similar to before, water-ice particles can be added in the bluer filter (RB/RC) to find the water-ice content. This is a comparable process to before, but with the potential added benefit of calibrating the images such that the radiances are not too high and the water-ice opacity can be found. If this is a successful alteration to the methods, many more image sequences can be analyzed to get a more complete picture of the water-ice optical depth. This is a feasible way to reanalyze this work, but it would require a substantial amount of reworking.

Another avenue of future work is to explore the representation of water-ice in the D&A model. Currently, water-ice particles are small, using Mie scattering to interact with the incoming radiation. Here, it would be advantageous to adjust the size of the particles to potentially better represent boundary layer clouds with larger particle radii (Whiteway et al., 2009). This would be achieved using a Henyey-Greenstein scattering approach. Allowing water-ice particle size to vary when matching the radiances may gave additional insight into the microphysical properties of the clouds.

Like with the analysis of cloud emission at other landing sites, the opacity of clouds can be studied by other surface spacecraft. This has been carried out at the MSL landing site (Kloos et al., 2018), but other sites with cameras, such as InSight, are missing this data from the surface that could help bring together a more global picture.

The most thorough understanding of water-ice clouds, and their effect on the climate through radiative transfer, however, requires a substantial increase in surface operations. While orbiters can cover a large surface area of the planet, the measurements are restricted by both their orbits, constraining the time of day when measurements are made, and their inability to resolve closely to the surface. Orbiters are not able to easily observe boundary layer clouds, for instance. With the landers that have operated on Mars up until this point, there remain large gaps in global coverage. For example, Spirit was the most southern-based lander, with a latitude of only 14.56°S. Increasing the number of missions on the surface of Mars is essential for further understanding the climate and dynamics of the Martian atmosphere.

References

Summers, M. E., Lieb, B. J., Chapman, E., & Yung, Y. L. (2002). Atmospheric biomarkers of subsurface life on mars. *Geophysical Research Letters*, *29*(24), 24–1–24–4. https://doi.org/10.1029/2002GL015377

Martínez, G. M., Newman, C. N., De Vicente-Retortillo, A., Fischer, E., Renno, N. O., Richardson, M. I., Fairén, A. G., Genzer, M., Guzewich, S. D., Haberle, R. M., Harri, A.-M., Kemppinen, O., Lemmon, M. T., Smith, M. D., de la Torre-Juárez, M., & Vasavada, A. R. (2017). The modern near-surface martian climate: A review of in-situ meteorological data from viking to curiosity. *Space Science Reviews*, *212*(1), 295–338. https://doi.org/10.1007/s11214-017-0360-x

Cantor, B. A., James, P. B., Caplinger, M., & Wolff, M. J. (2001). Martian dust storms: 1999 mars orbiter camera observations. *Journal of Geophysical Research: Planets*, *106*, 23653–23687. https://doi.org/10.1029/2000JE001310

Guzewich, S. D., Lemmon, M., Smith, C. L., Martínez, G., Vicente-Retortillo, Á. d., Newman, C. E., Baker, M., Campbell, C., Cooper, B., Gómez-Elvira, J., Harri, A.-M., Hassler, D., Martin-Torres, F. J., McConnochie, T., Moores, J. E., Kahanpää, H., Khayat, A., Richardson, M. I., Smith, M. D., . . . Mier, M.-P. Z. (2019). Mars science laboratory observations of the 2018/mars year 34 global dust storm. *Geophysical Research Letters*, *46*(1), 71–79. https://doi.org/https://doi.org/10.1029/2018GL080839

Clancy, R. T., Grossman, A. W., Wolff, M. J., James, P. B., Rudy, D. J., Billawala, Y. N., Sandor, B. J., Lee, S. W., & Muhleman, D. O. (1996). Water vapor saturation at low altitudes around mars aphelion: A key to mars climate? [ADS Bibcode: 1996Icar..122...36C]. *Icarus*, *122*, 36–62. https://doi.org/10.1006/icar.1996.0108

Christensen, P. R., Bandfield, J. L., Hamilton, V. E., Ruff, S. W., Kieffer, H. H., Titus, T. N., Malin, M. C., Morris, R. V., Lane, M. D., Clark, R. L., Jakosky, B. M., Mellon, M. T., Pearl, J. C., Conrath, B. J., Smith, M. D., Clancy, R. T., Kuzmin, R. O., Roush, T., Mehall, G. L., ... Greenfield, M. (2001). Mars global surveyor thermal emission spectrometer experiment: Investigation description and surface science results [ADS Bibcode: 2001JGR...10623823C]. *Journal of Geophysical Research*, *106*, 23823–23872. https://doi.org/10.1029/2000JE001370

Petrosyan, A., Galperin, B., Larsen, S. E., Lewis, S. R., Määttänen, A., Read, P. L., Renno, N., Rogberg, L. P. H. T., Savijärvi, H., Siili, T., Spiga, A., Toigo, A., & Vázquez, L. (2011). The martian atmospheric boundary layer. *Reviews of Geophysics*, *49*(3). https://doi.org/10.1029/2010RG000351

Guzewich, S. D., Newman, C. E., Smith, M. D., Moores, J. E., Smith, C. L., Moore, C., Richardson, M. I., Kass, D., Kleinböhl, A., Mischna, M., Martín-Torres, F. J., Zorzano-Mier, M.-P., & Battalio, M. (2017). The vertical dust profile over gale crater, mars. *Journal of Geophysical Research: Planets*, *122*(12), 2779–2792. https://doi.org/10.1002/2017JE005420

Dollfus, A. (1957). Étude des planètes par la polarisation de leur lumière [ADS Bibcode: 1957SAnAp...4....3D]. *Supplements aux Annales d'Astrophysique*, *4*, 3–114. Retrieved June 26, 2022, from https://ui.adsabs.harvard.edu/abs/1957SAnAp...4....3D

Pollack, J., & Sagan, C. (1969). An analysis of martian photometry and polarimetry. *Space Science Reviews*, *9*(2), 243–299. https://doi.org/10.1007/BF00215634

Vago, J., Witasse, O., Svedhem, H., Baglioni, P., Haldemann, A., Gianfiglio, G., Blancquaert, T., McCoy, D., & de Groot, R. (2015). ESA ExoMars program: The next step in exploring mars [ADS Bibcode: 2015SoSyR..49..518V]. *Solar System Research*, *49*, 518–528. https://doi.org/10.1134/S0038094615070199

Schmidt, R. (2003). Mars express—ESA's first mission to planet mars. *Acta Astronautica*, *52*(2), 197–202. https://doi.org/10.1016/S0094-5765(02)00157-1

Graf, J. E., Zurek, R. W., Eisen, H. J., Jai, B., Johnston, M. D., & DePaula, R. (2005). The mars reconnaissance orbiter mission. *Acta Astronautica*, *57*(2), 566–578. https://doi.org/10.1016/j.actaastro.2005.03.043

Taylor, P. A., Catling, D. C., Daly, M., Dickinson, C. S., Gunnlaugsson, H. P., Harri, A.-M., & Lange, C. F. (2008). Temperature, pressure, and wind instrumentation in the phoenix meteorological package. *Journal of Geophysical Research: Planets*, *113, E00A10*. https://doi.org/10.1029/2007JE003015

Grotzinger, J. P., Crisp, J., Vasavada, A. R., Anderson, R. C., Baker, C. J., Barry, R., Blake, D. F., Conrad, P., Edgett, K. S., Ferdowski, B., Gellert, R., Gilbert, J. B., Golombek, M., Gómez-Elvira, J., Hassler, D. M., Jandura, L., Litvak, M., Mahaffy, P., Maki, J., … Wiens, R. C. (2012). Mars science laboratory mission and science investigation. *Space Science Reviews*, *170*(1), 5–56. https://doi.org/10.1007/s11214-012-9892-2

Farley, K. A., Williford, K. H., Stack, K. M., Bhartia, R., Chen, A., de la Torre, M., Hand, K., Goreva, Y., Herd, C. D. K., Hueso, R., Liu, Y., Maki, J. N., Martinez, G., Moeller, R. C., Nelessen, A., Newman, C. E., Nunes, D., Ponce, A., Spanovich, N., … Wiens, R. C. (2020). Mars 2020 mission overview [ADS Bibcode: 2020SSRv..216..142F]. *Space Science Reviews*, *216*, 142. https://doi.org/10.1007/s11214-020-00762-y

Määttänen, A., & Montmessin, F. (2021, April 26). *Clouds in the martian atmosphere* [Oxford research encyclopedia of planetary science] [ISBN: 9780190647926]. https://doi.org/10.1093/acrefore/9780190647926.013.114

Richardson, M. I., Wilson, R. J., & Rodin, A. V. (2002). Water ice clouds in the martian atmosphere: General circulation model experiments with a simple cloud scheme. *Journal of Geophysical Research: Planets*, *107*, 2–1–2–29. https://doi.org/10.1029/2001JE001804

Smith. (2019). Local time variation of water ice clouds on mars as observed by THEMIS. *Icarus*, *333*, 273–282. https://doi.org/10.1016/j.icarus.2019.06.009

Kloos, J. L., Moores, J. E., Whiteway, J. A., & Aggarwal, M. (2018). Interannual and diurnal variability in water ice clouds observed from MSL over two martian years. *Journal of Geophysical Research: Planets*, *123*(1), 233–245. https://doi.org/10.1002/2017JE005314

Cooper, Moores, J. E., Ellison, D. J., Kloos, J. L., Smith, C. L., Guzewich, S. D., & Campbell, C. L. (2019). Constraints on mars aphelion cloud belt phase function and ice crystal geometries. *Planetary and Space Science*, *168*, 62–72. https://doi.org/10.1016/j.pss.2019.01.005

Martin, L. J., & McKinney, W. M. (1974). North polar hood of mars in 1969 (may 18-july 25). i. blue light [ADS Bibcode: 1974Icar...23..380M]. *Icarus*, *23*, 380–387. https://doi.org/10.1016/0019-1035(74)90056-6

Benson, J. L., Kass, D. M., & Kleinböhl, A. (2011). Mars' north polar hood as observed by the mars climate sounder. *Journal of Geophysical Research: Planets*, *116, E03008*. https://doi.org/10.1029/2010JE003693

Tamppari, L. K., Smith, M. D., Bass, D. S., & Hale, A. S. (2008). Water-ice clouds and dust in the north polar region of mars using MGS TES data. *Planetary and Space Science*, *56*(2), 227–245. https://doi.org/10.1016/j.pss.2007.08.011

Sánchez-Lavega, A., Garro, A., del Río-Gaztelurrutia, T., Hueso, R., Ordoñez-Etxeberria, I., Chen Chen, H., Cardesín-Moinelo, A., Titov, D., Wood, S., Almeida, M., Spiga, A., Forget, F., Määttänen, A., Hoffmann, H., & Gondet, B. (2018). A seasonally recurrent annular cyclone in mars northern latitudes and observations of a companion vortex. *Journal of Geophysical Research: Planets*, *123*(11), 3020–3034. https://doi.org/10.1029/2018JE005740

Tamppari, L. K., Bass, D., Cantor, B., Daubar, I., Dickinson, C., Fisher, D., Fujii, K., Gunnlauggson, H. P., Hudson, T. L., Kass, D., Kleinböhl, A., Komguem, L., Lemmon, M. T., Mellon, M., Moores, J., Pankine, A., Pathak, J., Searls, M., Seelos, F., … Wolff, M. (2010). Phoenix and MRO coordinated atmospheric measurements. *Journal of Geophysical Research: Planets*, *115, E00E17*. https://doi.org/https://doi.org/10.1029/2009JE003415

Tyler, D., & Barnes, J. R. (2014). Atmospheric mesoscale modeling of water and clouds during northern summer on mars. *Icarus*, *237*, 388–414. https://doi.org/10.1016/j.icarus.2014.04.020

Montmessin, F., Forget, F., Rannou, P., Cabane, M., & Haberle, R. M. (2004). Origin and role of water ice clouds in the martian water cycle as inferred from a general circulation model. *Journal of Geophysical Research: Planets*, *109*. https://doi.org/10.1029/2004JE002284

Tamppari, L. K., Zurek, R. W., & Paige, D. A. (2003). Viking-era diurnal water-ice clouds. *Journal of Geophysical Research: Planets*, *108*. https://doi.org/10.1029/2002JE001911

Wilson, R. J., Neumann, G. A., & Smith, M. D. (2007). Diurnal variation and radiative influence of martian water ice clouds. *Geophysical Research Letters*, *34, L02710*(2). https://doi.org/https://doi.org/10.1029/2006GL027976

Madeleine, J.-B., Forget, F., Spiga, A., Wolff, M. J., Montmessin, F., Vincendon, M., Jouglet, D., Gondet, B., Bibring, J.-P., Langevin, Y., & Schmitt, B. (2012). Aphelion water-ice cloud mapping and property retrieval using the OMEGA imaging spectrometer onboard mars express. *Journal of Geophysical Research: Planets*, *117, E00J07*. https://doi.org/10.1029/2011JE003940

Moores, J. E., Lemmon, M. T., Smith, P. H., Komguem, L., & Whiteway, J. A. (2010). Atmospheric dynamics at the phoenix landing site as seen by the surface stereo imager. *Journal of Geophysical Research: Planets*, *115, E00E08*. https://doi.org/https://doi.org/10.1029/2009JE003409

Savijärvi, H. (2014). A toy climate model for mars. *Icarus*, *242*, 105–111. https://doi.org/10.1016/j.icarus.2014.07.029

Madeleine, J.-B., Forget, F., Millour, E., Montabone, L., & Wolff, M. J. (2011). Revisiting the radiative impact of dust on mars using the LMD global climate model. *Journal of Geophysical Research: Planets*, *116, E11010*. https://doi.org/https://doi.org/10.1029/2011JE003855

Kuo, H. L. (1961). Convection in conditionally unstable atmosphere. *Tellus*, *13*(4), 441–459. https://doi.org/10.3402/tellusa.v13i4.9516

Hong, Y., Liu, G., & Li, J.-L. F. (2016). Assessing the radiative effects of global ice clouds based on CloudSat and CALIPSO measurements [Publisher: American Meteorological Society Section: Journal of Climate]. *Journal of Climate*, *29*(21), 7651–7674. https://doi.org/10.1175/JCLI-D-15-0799.1

Colaprete, A., & Toon, O. B. (2000). The radiative effects of martian water ice clouds on the local atmospheric temperature profile. *Icarus*, *145*(2), 524–532. https://doi.org/10.1006/icar.2000.6364

Hinson, & Wilson, R. J. (2004). Temperature inversions, thermal tides, and water ice clouds in the martian tropics [_eprint: https://onlinelibrary.wiley.com/doi/pdf/10.1029/2003JE002129]. *Journal of Geophysical Research: Planets*, *109*. https://doi.org/10.1029/2003JE002129

Wilson, R. J., & Guzewich, S. D. (2014). Influence of water ice clouds on nighttime tropical temperature structure as seen by the mars climate sounder. *Geophysical Research Letters*, *41*(10), 3375–3381. https://doi.org/10.1002/2014GL060086

Cooper, de la Torre Juárez, M., Mischna, M., Lemmon, M., Martínez, G., Kass, D., Vasavada, A. R., Campbell, C., & Moores, J. (2021). Thermal forcing of the nocturnal near surface environment by martian water ice clouds. *Journal of Geophysical Research: Planets*, *126*(12), e2020JE006737. https://doi.org/10.1029/2020JE006737

Smith, Tamppari, L., Arvidson, R. E., Bass, D., Blaney, D., Boynton, W., Carswell, A., Catling, D., Clark, B., Duck, T., DeJong, E., Fisher, D., Goetz, W., Gunnlaugsson, P., Hecht, M., Hipkin, V., Hoffman, J., Hviid, S., Keller, H., ... Zent, A. (2008). Introduction to special section on the phoenix mission: Landing site characterization experiments, mission overviews, and expected science [_eprint: https://agupubs.onlinelibrary.wiley.com/doi/pdf/10.1029/20 *Journal of Geophysical Research: Planets*, *113*. https://doi.org/10.1029/2008JE003083

Whiteway, Daly, M., Carswell, A., Duck, T., Dickinson, C., Komguem, L., & Cook, C. (2008). Lidar on the phoenix mission to mars. *Journal of Geophysical Research: Planets*, *113*. https://doi.org/10.1029/2007JE003002

Komguem, L., Whiteway, J. A., Dickinson, C., Daly, M., & Lemmon, M. T. (2013). Phoenix LIDAR measurements of mars atmospheric dust. *Icarus*, *223*(2), 649–653. https://doi.org/10.1016/j.icarus.2013.01.020

Dickinson, C., Whiteway, J. A., Komguem, L., Moores, J. E., & Lemmon, M. T. (2010). Lidar measurements of clouds in the planetary boundary layer on mars. *Geophysical Research Letters*, *37, L18203*(18). https://doi.org/https://doi.org/10.1029/2010GL044317

Whiteway, Komguem, L., Dickinson, C., Cook, C., Illnicki, M., Seabrook, J., Popovici, V., Duck, T. J., Davy, R., Taylor, P. A., Pathak, J., Fisher, D., Carswell, A. I., Daly, M., Hipkin, V., Zent, A. P., Hecht, M. H., Wood, S. E., Tamppari, L. K., ... Smith, P. H. (2009). Mars water-ice clouds and precipitation. *Science*, *325*(5936), 68–70. https://doi.org/10.1126/science.1172344

Mellon, M. T., Arvidson, R. E., Sizemore, H. G., Searls, M. L., Blaney, D. L., Cull, S., Hecht, M. H., Heet, T. L., Keller, H. U., Lemmon, M. T., Markiewicz, W. J., Ming, D. W., Morris, R. V., Pike, W. T., & Zent, A. P. (2009). Ground ice at the phoenix landing site: Stability state and origin. *Journal of Geophysical Research: Planets*, *114, E00E07*. https://doi.org/https://doi.org/10.1029/2009JE003417

Moores, J. E., Komguem, L., Whiteway, J. A., Lemmon, M. T., Dickinson, C., & Daerden, F. (2011). Observations of near-surface fog at the phoenix mars landing site [_eprint: https://agupubs.onlinelibrary.wiley.com/doi/pdf/10.1029/2010GL046315]. *Geophysical Research Letters*, *38, L04203*(4). https://doi.org/https://doi.org/10.1029/2010GL046315

Moores, J. E., Lemmon, M. T., Rafkin, S. C. R., Francis, R., Pla-Garcia, J., de la Torre Juárez, M., Bean, K., Kass, D., Haberle, R., Newman, C., Mischna, M., Vasavada, A., Rennó, N., Bell, J., Calef, F., Cantor, B., Mcconnochie, T. H., Harri, A.-M., Genzer, M., ... McCullough, E. (2015). Atmospheric movies acquired at the mars science laboratory landing site: Cloud morphology, frequency and significance to the gale crater water cycle and phoenix mission results. *Advances in Space Research*, *55*(9), 2217–2238. https://doi.org/10.1016/j.asr.2015.02.007

Gunnlaugsson, H. P., Holstein-Rathlou, C., Merrison, J. P., Knak Jensen, S., Lange, C. F., Larsen, S. E., Madsen, M. B., Nørnberg, P., Bechtold, H., Hald, E., Iversen, J. J., Lange, P., Lykkegaard, F., Rander, F., Lemmon, M., Renno, N., Taylor, P., & Smith, P. (2008). Telltale wind indicator for the mars phoenix lander. *Journal of Geophysical Research: Planets*, *113, E00A04*. https://doi.org/10.1029/2007JE003008

Davy, R., Davis, J. A., Taylor, P. A., Lange, C. F., Weng, W., Whiteway, J., & Gunnlaugson, H. P. (2010). Initial analysis of air temperature and related data from the phoenix MET station and their use in estimating turbulent heat fluxes. *Journal of Geophysical Research: Planets*, *115, E00E13*. https://doi.org/https://doi.org/10.1029/2009JE003444

Vicente-Retortillo, Á., Valero, F., Vázquez, L., & Martínez, G. M. (2015). A model to calculate solar radiation fluxes on the martian surface [Publisher: EDP Sciences]. *Journal of Space Weather and Space Climate*, *5*, A33. https://doi.org/10.1051/swsc/2015035

Savijärvi, H., & Määttänen, A. (2010). Boundary-layer simulations for the mars phoenix lander site. *Quarterly Journal of the Royal Meteorological Society*, *136*(651), 1497–1505. https://doi.org/https://doi.org/10.1002/qj.650

Christensen, P. R., Wyatt, M. B., Glotch, T. D., Rogers, A. D., Anwar, S., Arvidson, R. E., Bandfield, J. L., Blaney, D. L., Budney, C., Calvin, W. M., Fallacaro, A., Fergason, R. L., Gorelick, N., Graff, T. G., Hamilton, V. E., Hayes, A. G., Johnson, J. R., Knudson, A. T., McSween, H. Y., . . . Wolff, M. J. (2004). Mineralogy at meridiani planum from the mini-TES experiment on the opportunity rover [Publisher: American Association for the Advancement of Science]. *Science*, *306*(5702), 1733–1739. https://doi.org/10.1126/science.1104909

Martínez, G. M., Rennó, N., Fischer, E., Borlina, C. S., Hallet, B., Juárez, M. d. l. T., Vasavada, A. R., Ramos, M., Hamilton, V., Gomez-Elvira, J., & Haberle, R. M. (2014). Surface energy budget and thermal inertia at gale crater: Calculations from ground-based measurements. *Journal of Geophysical Research: Planets*, *119*(8), 1822–1838. https://doi.org/https://doi.org/10.1002/2014JE004618

Mellon, M. T., Jakosky, B. M., Kieffer, H. H., & Christensen, P. R. (2000). High-resolution thermal inertia mapping from the mars global surveyor thermal emission spectrometer. *Icarus*, *148*(2), 437–455. https://doi.org/10.1006/icar.2000.6503

Zent, A., Hecht, M., Cobos, D., Wood, S., Hudson, T., Milkovich, S., Deflores, L., & Mellon, M. (2010). Initial results from the thermal and electrical conductivity probe (TECP) on phoenix. *Journal of Geophysical Research, 115, E00E14*. https://doi.org/10.1029/2009JE003420

Schorghofer, N. (2005). Stability and exchange of subsurface ice on mars. *Journal of Geophysical Research*, *110*, E05003. https://doi.org/10.1029/2004JE002350

Holstein-Rathlou, C., Gunnlaugsson, H. P., Merrison, J. P., Bean, K. M., Cantor, B. A., Davis, J. A., Davy, R., Drake, N. B., Ellehoj, M. D., Goetz, W., Hviid, S. F., Lange, C. F., Larsen, S. E., Lemmon, M. T., Madsen, M. B., Malin, M., Moores, J. E., Nørnberg, P., Smith, P., … Taylor, P. A. (2010). Winds at the phoenix landing site. *Journal of Geophysical Research: Planets*, *115, E00E18*. https://doi.org/https://doi.org/10.1029/2009JE003411

Smith, Wolff, M. J., Spanovich, N., Ghosh, A., Banfield, D., Christensen, P. R., Landis, G. A., & Squyres, S. W. (2006). One martian year of atmospheric observations using MER mini-TES. *Journal of Geophysical Research: Planets*, *111*. https://doi.org/10.1029/2006JE002770

Press, W. H., Teukolsky, S. A., Vetterling, W. T., & Flannery, B. P. (1992). Numerical recipes in c. *Numerical recipes in c: The art of scientific computing* (2nd Edition). Cambridge University Press.

Chevrier, V. F., Hanley, J., & Altheide, T. S. (2009). Stability of perchlorate hydrates and their liquid solutions at the phoenix landing site, mars. *Geophysical Research Letters*, *36, L10202*(10). https://doi.org/10.1029/2009GL037497

Nikolakakos, G., & Whiteway, J. A. (2015). Laboratory investigation of perchlorate deliquescence at the surface of mars with a raman scattering lidar. *Geophysical Research Letters*, *42*(19), 7899–7906. https://doi.org/10.1002/2015GL065434

Wendisch, M., Yang, P., & Pilewskie, P. (2007). Effects of ice crystal habit on thermal infrared radiative properties and forcing of cirrus. *Journal of Geophysical Research: Atmospheres*, *112*. https://doi.org/10.1029/2006JD007899

Cooper, Moores, J. E., Battalio, J. M., Guzewich, S. D., Smith, C. L., Modestino, R. C. N., & Tabascio, M. V. (2020). Aphelion cloud belt phase function investigations with mars color imager (MARCI). *Planetary and Space Science*, *184*, 104840. https://doi.org/10.1016/j.pss.2020.104840

Guo, L., Guo, X., Luan, T., Zhu, S., & Lyu, K. (2021). Radiative effects of clouds and fog on long-lasting heavy fog events in northern china. *Atmospheric Research*, *252*, 105444. https://doi.org/10.1016/j.atmosres.2020.105444

Hinson, Wang, H., Wilson, J., & Spiga, A. (2021). Nighttime convection in water-ice clouds at high northern latitudes on mars. *Icarus*, 114693. https://doi.org/10.1016/j.icarus.2021.114693

Spiga, A., Hinson, D. P., Madeleine, J.-B., Navarro, T., Millour, E., Forget, F., & Montmessin, F. (2017). Snow precipitation on mars driven by cloud-induced night-time convection [Number: 9 Publisher: Nature Publishing Group]. *Nature Geoscience*, *10*(9), 652–657. https://doi.org/10.1038/ngeo3008

Lemmon, M. T., Smith, P., Shinohara, C., Tanner, R., Woida, P., Shaw, A., & Hughes, J. (2008). The phoenix surface stereo imager (SSI) investigation.

Tomasko, M. G., Doose, L. R., Smith, P. H., & Odell, A. P. (1980). Measurements of the flux of sunlight in the atmosphere of venus. *Journal of Geophysical Research: Space Physics*, *85*, 8167–8186. https://doi.org/10.1029/JA085iA13p08167

Tomasko, M. G., Doose, L. R., Lemmon, M., Smith, P. H., & Wegryn, E. (1999). Properties of dust in the martian atmosphere from the imager on mars pathfinder. *Journal of Geophysical Research: Planets*, *104*, 8987–9007. https://doi.org/https://doi.org/10.1029/1998JE900016

Smith, & Moores, J. E. (2020). Modelled small-scale crack orientations in martian surface clasts caused by differential insolation-mobilized water. *Icarus*, *338*, 113497. https://doi.org/10.1016/j.icarus.2019.113497

Hansen, J. E. (1971). Multiple scattering of polarized light in planetary atmospheres. part i. the doubling method [Publisher: American Meteorological Society Section: Journal of the Atmospheric Sciences]. *Journal of the Atmospheric Sciences*, *28*(1), 120–125. https://doi.org/10.1175/1520-0469(1971)028<0120:MSOPLI>2.0.CO;2

Hansen, J. E., & Travis, L. D. (1974). Light scattering in planetary atmospheres [ADS Bibcode: 1974SSRv...16..527H]. *Space Science Reviews*, *16*, 527–610. https://doi.org/10.1007/BF00168069

Allen, C. W., & Cox, A. N. (2000). *Allen's astrophysical quantities* [Google-Books-ID: w8PK2XFLLH8C]. Springer Science & Business Media.

Wolff, M. J., Smith, M. D., Clancy, R. T., Arvidson, R., Kahre, M., Seelos IV, F., Murchie, S., & Savijärvi, H. (2009). Wavelength dependence of dust aerosol single scattering albedo as observed by the compact reconnaissance imaging spectrometer. *Journal of Geophysical Research: Planets*, *114*. https://doi.org/10.1029/2009JE003350

Johnson, J. R., Grundy, W. M., & Lemmon, M. T. (2003). Dust deposition at the mars pathfinder landing site: Observations and modeling of visible/near-infrared spectra. *Icarus*, *163*(2), 330–346. https://doi.org/10.1016/S0019-1035(03)00084-8

Kokhanovsky, A. (2004). Optical properties of terrestrial clouds. *Earth-Science Reviews*, *64*(3), 189–241. https://doi.org/10.1016/S0012-8252(03)00042-4

Guzewich, S. D., & Smith, M. D. (2019). Seasonal variation in martian water ice cloud particle size [_eprint: https://onlinelibrary.wiley.com/doi/pdf/10.1029/2018JE005843]. *Journal of Geophysical Research: Planets*, *124*(2), 636–643. https://doi.org/10.1029/2018JE005843

ASTM. (2000). *Standard solar constant and zero air mass solar spectral irradiance tables*. Retrieved July 20, 2022, from https://www.astm.org/e0490-22.html

Spiga, A., Banfield, D., Teanby, N. A., Forget, F., Lucas, A., Kenda, B., Rodriguez Manfredi, J. A., Widmer-Schnidrig, R., Murdoch, N., Lemmon, M. T., Garcia, R. F., Martire, L., Karatekin, Ö., Le Maistre, S., Van Hove, B., Dehant, V., Lognonné, P., Mueller, N., Lorenz, R., ... Banerdt, W. B. (2018). Atmospheric science with InSight. *Space Science Reviews*, *214*(7), 109. https://doi.org/10.1007/s11214-018-0543-0

Rodriguez-Manfredi, J. A., de la Torre Juárez, M., Alonso, A., Apéstigue, V., Arruego, I., Atienza, T., Banfield, D., Boland, J., Carrera, M. A., Castañer, L., Ceballos, J., Chen-Chen, H., Cobos, A., Conrad, P. G., Cordoba, E., del Río-Gaztelurrutia, T., de Vicente-Retortillo, A., Domínguez-Pumar, M., Espejo, S., ... The MEDA team. (2021). The mars environmental dynamics analyzer, MEDA. a suite of environmental sensors for the mars 2020 mission. *Space Science Reviews*, *217*(3), 48. https://doi.org/10.1007/s11214-021-00816-9